

WL - TR - 96 - 3069



**Measured AEDC Tunnel B and Predicted Linear Stability Theory Transition  
Comparison Study for a 7-degree Sharp Cone**

**Albert A. Rougeux**

**March 1996**

**Final Report for Period October 1995 to March 1996**

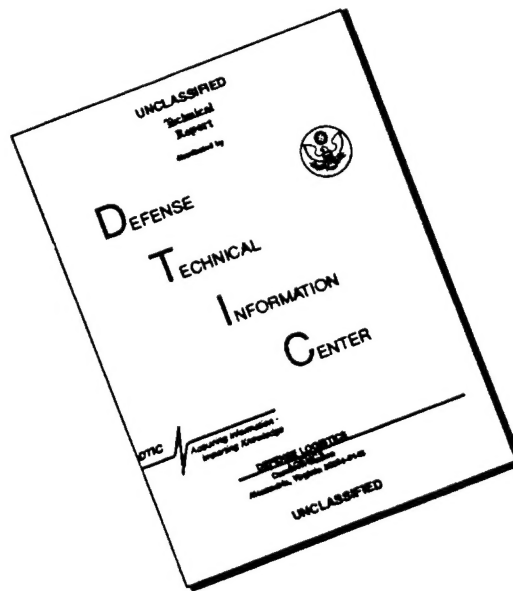
APPROVED FOR PUBLIC RELEASE; DISTRIBUTION IS UNLIMITED

FLIGHT DYNAMICS DIRECTORATE  
WRIGHT LABORATORY  
AIR FORCE MATERIEL COMMAND  
WRIGHT-PATTERSON AIR FORCE BASE, OHIO 45433-7562

19960708 033

DTIC QUALITY INSPECTED 1

# DISCLAIMER NOTICE



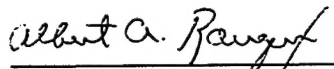
THIS DOCUMENT IS BEST QUALITY AVAILABLE. THE COPY FURNISHED TO DTIC CONTAINED A SIGNIFICANT NUMBER OF PAGES WHICH DO NOT REPRODUCE LEGIBLY.

## NOTICE

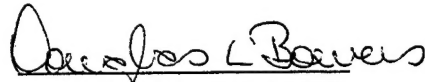
WHEN GOVERNMENT DRAWINGS, SPECIFICATIONS, OR OTHER DATA ARE USED FOR ANY PURPOSE OTHER THAN IN CONNECTION WITH A DEFINITELY GOVERNMENT-RELATED PROCUREMENT, THE UNITED STATES GOVERNMENT INCURS NO RESPONSIBILITY OR ANY OBLIGATION WHATSOEVER, THE FACT THAT THE GOVERNMENT MAY HAVE FORMULATED OR IN ANY WAY SUPPLIED THE SAID DRAWINGS, SPECIFICATIONS, OR OTHER DATA, IS NOT TO BE REGARDED BY IMPLICATION, OR OTHERWISE IN ANY MANNER CONSTRUED, AS LICENSING THE HOLDER, OR ANY OTHER PERSON OR CORPORATION; OR AS CONVEYING ANY RIGHTS OR PERMISSION TO MANUFACTURE, USE, SELL ANY PATENTED INVENTION THAT MAY IN ANY WAY BE RELATED THERETO.

THIS REPORT IS RELEASABLE TO THE NATIONAL TECHNICAL INFORMATION SERVICE (NTIS). AT NTIS, IT WILL BE DISTRIBUTED TO THE GENERAL PUBLIC.

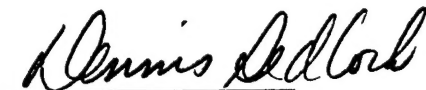
THIS TECHNICAL REPORT HAS BEEN REVIEWED AND IS APPROVED FOR PUBLICATION.



ALBERT A. ROUGEUX  
Aerospace Engineer  
Aerothermodynamics Research Section



DOUGLAS L. BOWERS  
Acting Chief  
Aerodynamics and Aero Components  
Research Branch



DENNIS SEDLOCK  
Chief  
Aeromechanics Division

IF YOUR ADDRESS HAS CHANGED, IF YOU WISH TO BE REMOVED FROM OUR MAILING LIST, OR IF THE ADDRESSEE IS NO LONGER EMPLOYED BY YOUR ORGANIZATION PLEASE NOTIFY WL/FIMA, WRIGHT-PATTERSON AFB, OH 45433-7913 TO HELP MAINTAIN A CURRENT MAILING LIST.

COPIES OF THIS REPORT SHOULD NOT BE RETURNED UNLESS RETURN IS REQUIRED BY SECURITY CONSIDERATIONS, CONTRACTUAL OBLIGATIONS, OR NOTICE ON A SPECIFIC DOCUMENT.

REPORT DOCUMENTATION PAGE			Form Approved OMB No. 0704-0188	
Public reporting burden for this collection of information is estimated to average 1 hour per response, including the time for reviewing instructions, searching existing data sources, gathering and maintaining the data needed, and completing and reviewing the collection of information. Send comments regarding this burden estimate or any other aspect of this collection of information, including suggestions for reducing this burden, to Washington Headquarters Services, Directorate for Information Operations and Reports, 1215 Jefferson Davis Highway, Suite 1204, Arlington, VA 22202-4302, and to the Office of Management and Budget, Paperwork Reduction Project (0704-0188), Washington, DC 20503.				
1. AGENCY USE ONLY (Leave blank)		2. REPORT DATE Mar 1996		3. REPORT TYPE AND DATES COVERED Final for Oct 1995 to Mar 1996
4. TITLE AND SUBTITLE Measured AEDC Tunnel B and Predicted Linear Stability Theory Transition Comparison Study for a 7-degree Sharp Cone			5. FUNDING NUMBERS PE: 62201F PR: 2404 TA: 07 WU: A5	
6. AUTHOR(S) Albert A. Rougeux				
7. PERFORMING ORGANIZATION NAME(S) AND ADDRESS(ES) Flight Dynamics Directorate Wright Laboratory Air Force Materiel Command Wright-Patterson AFB OH 45433-7562			8. PERFORMING ORGANIZATION REPORT NUMBER	
9. SPONSORING/MONITORING AGENCY NAME(S) AND ADDRESS(ES) Flight Dynamics Directorate Wright Laboratory Air Force Materiel Command Wright-Patterson AFB OH 45433-7562 POC: A.A. Rougeux, WL/FIMA, 255-2021			10. SPONSORING/MONITORING AGENCY REPORT NUMBER  WL - TR - 96 - 3069	
11. SUPPLEMENTARY NOTES				
12a. DISTRIBUTION / AVAILABILITY STATEMENT APPROVED FOR PUBLIC RELEASE; DISTRIBUTION IS UNLIMITED			12b. DISTRIBUTION CODE	
13. ABSTRACT (Maximum 200 words) The location of the stability region between the laminar and turbulent flow is of great importance in the design of high speed missiles and aircraft's. Heat transfer and skin friction vary greatly between laminar and turbulent, therefore, transition location is indispensable for predicting vehicle performance. The boundary layer stability of a sharp, 7-degree half angle cone with freestream Mach numbers of 6 and 8 was numerically investigated using linear stability theory computer program. Results were compared with wind tunnel tests results obtained at the AEDC Von Karman Hypersonic Tunnel B. Measured and computed frequencies agree well, indicating that linear stability theory properly describes the processes leading to transition at the AEDC Tunnel B.				
14. SUBJECT TERMS Linear Stability, Transition, Hypersonic, Laminar, Experiment			15. NUMBER OF PAGES 54	
			16. PRICE CODE	
17. SECURITY CLASSIFICATION OF REPORT Unclassified	18. SECURITY CLASSIFICATION OF THIS PAGE Unclassified	19. SECURITY CLASSIFICATION OF ABSTRACT Unclassified	20. LIMITATION OF ABSTRACT SAR	



## CONTENTS

<b>1.0 INTRODUCTION</b>	<b>1</b>
<b>2.0 EXPERIMENTAL CONFIGURATION</b>	<b>3</b>
<b>3.0 COMPUTER CODE E - MALIK</b>	<b>4</b>
<b>4.0 SPATIAL THEORY</b>	<b>5</b>
<b>5.0 NUMERICAL COMPUTATIONS</b>	<b>8</b>
<b>6.0 GENERAL RESULTS</b>	<b>9</b>
<b>7.0 CONCLUSIONS</b>	<b>13</b>
<b>8.0 REFERENCES</b>	<b>14</b>
<b>APPENDIX A</b>	<b>16</b>

## LIST OF FIGURES

FIGURE A 1 EXPERIMENTAL SETUP AEDC TUNNEL B .....	16
FIGURE A 2 HOT-WIRE ANEMOMETER PROFILE.....	16
FIGURE A 3 BOUNDARY LAYER FLUCTUATION SPECTRA.....	17
FIGURE A 4 FLUCTUATION SPECTRA OVERLAID .....	17
FIGURE A 5 N-FACTOR CURVES, $M=8.0$ , ADIABATIC.....	18
FIGURE A 6 N-FACTOR CURVES, $M=8.0$ , $T_w/T_o=0.41$ .....	18
FIGURE A 7 N-FACTOR CURVES, $M=6.0$ , $T_w/T_o=0.63$ .....	19
FIGURE A 8 N-FACTOR CURVES, $M=6.0$ , $T_w/T_o=0.41$ .....	19
FIGURE A 9 MAG. PRESSURE EIGENFUNCTION, $M=8.0$ , ADIABATIC .....	20
FIGURE A 10 MAG. PRESSURE EIGENFUNCTION, $M=8.0$ , $T_w/T_o=0.41$ .....	20
FIGURE A 11 MAG. PRESSURE EIGENFUNCTION, $M=6.0$ , $T_w/T_o=0.63$ .....	21
FIGURE A 12 MAG. PRESSURE EIGENFUNCTION, $M=6.0$ , $T_w/T_o=0.41$ .....	21
FIGURE A 13 TEMPERATURE EIGENFUNCTION, $M=8.0$ , ADIABATIC.....	22
FIGURE A 14 TEMPERATURE EIGENFUNCTION, $M=8.0$ , $T_w/T_o=0.41$ .....	22
FIGURE A 15 TEMPERATURE EIGENFUNCTION, $M=6.0$ , $T_w/T_o=0.63$ .....	23
FIGURE A 16 TEMPERATURE EIGENFUNCTION $M=6.0$ , $T_w/T_o=0.41$ .....	23
FIGURE A 17. MASS EIGENFUNCTION, $M=8.0$ , ADIABATIC .....	24
FIGURE A 18 MASS EIGENFUNCTION, $M=8.0$ , $T_w/T_o=0.41$ .....	24
FIGURE A 19 MASS EIGENFUNCTION, $M=6.0$ , $T_w/T_o=0.63$ .....	25
FIGURE A 20 MASS EIGENFUNCTION, $M=6.0$ , $T_w/T_o=0.41$ .....	25
FIGURE A 21 PRESSURE FUNCTION PHASE ANGLE, $M=8.0$ , ADIABATIC .....	26
FIGURE A 22 PRESSURE FUNCTION PHASE ANGLE, $M=8.0$ , $T_w/T_o=0.41$ .....	26
FIGURE A 23 PRESSURE FUNCTION PHASE ANGLE, $M=6.0$ , $T_w/T_o=0.63$ .....	27
FIGURE A 24 PRESSURE FUNCTION PHASE ANGLE, $M=6.0$ , $T_w/T_o=0.41$ .....	27
FIGURE A 25 TEMPERATURE FUNCTION PHASE ANGLE, $M=8.0$ , ADIABATIC .....	28
FIGURE A 26 TEMPERATURE FUNCTION PHASE ANGLE, $M=8.0$ , $T_w/T_o = 0.41$ .....	28
FIGURE A 27 TEMPERATURE FUNCTION PHASE ANGLE, $M=6.0$ , $T_w/T_o = 0.63$ .....	29
FIGURE A 28 TEMPERATURE FUNCTION PHASE ANGLE, $M=6.0$ , $T_w/T_o = 0.41$ .....	29
FIGURE A 29 MASS FUNCTION PHASE ANGLE, $M=8.0$ , ADIABATIC .....	30
FIGURE A 30 MASS FUNCTION PHASE ANGLE, $M=8.0$ , $T_w/T_o = 0.41$ .....	30
FIGURE A 31 MASS FUNCTION PHASE ANGLE, $M=6.0$ , $T_w/T_o = 0.63$ .....	31
FIGURE A 32 MASS FUNCTION PHASE ANGLE, $M=6.0$ , $T_w/T_o = 0.41$ .....	31
FIGURE A 33 REAL PART PRESSURE FUNCTION, $M=8.0$ , ADIABATIC.....	32
FIGURE A 34 REAL PART PRESSURE FUNCTION, $M=8.0$ , $T_w/T_o = 0.41$ .....	32
FIGURE A 35 REAL PART PRESSURE FUNCTION, $M=6.0$ , $T_w/T_o = 0.63$ .....	33
FIGURE A 36 REAL PART PRESSURE FUNCTION, $M=6.0$ , $T_w/T_o=0.41$ .....	33
FIGURE A 37 REAL PART TEMPERATURE FUNCTION, $M=8.0$ , ADIABATIC .....	34
FIGURE A 38 REAL PART TEMPERATURE FUNCTION, $M=8.0$ , $T_w/T_o = 0.41$ .....	34
FIGURE A 39 REAL PART TEMPERATURE FUNCTION, $M=6.0$ , $T_w/T_o = 0.63$ .....	35
FIGURE A 40 REAL PART TEMPERATURE FUNCTION, $M=6.0$ , $T_w/T_o = 0.41$ .....	35
FIGURE A 41 REAL PART MASS FUNCTION, $M=8.0$ , ADIABATIC.....	36
FIGURE A 42 REAL PART MASS FUNCTION, $M=8.0$ , $T_w/T_o = 0.41$ .....	36
FIGURE A 43 REAL PART MASS FUNCTION, $M=6.0$ , $T_w/T_o = 0.63$ .....	37
FIGURE A 44 REAL PART MASS FUNCTION, $M=6.0$ , $T_w/T_o = 0.41$ .....	37
FIGURE A 45 REAL PART MASS FUNCTION, $M=8.0$ , ADIABATIC.....	38
FIGURE A 46 REAL PART MASS FUNCTION, $M=8.0$ , $T_w/T_o = 0.41$ .....	38
FIGURE A 47 REAL PART MASS FUNCTION, $M=6.0$ , $T_w/T_o = 0.63$ .....	39
FIGURE A 48 REAL PART MASS FUNCTION, $M=6.0$ , $T_w/T_o = 0.41$ .....	39
FIGURE A 49 REAL PART MASS FUNCTION, $M=8.0$ , ADIABATIC.....	40
FIGURE A 50 REAL PART MASS FUNCTION, $M=6.0$ , $T_w/T_o = 0.41$ .....	40
FIGURE A 51 REAL PART MASS FUNCTION, $M=6.0$ , $T_w/T_o = 0.63$ .....	41
FIGURE A 52 REAL PART MASS FUNCTION, $M=6.0$ , $T_w/T_o = 0.41$ .....	41

## LIST OF TABLES

TABLE 1 AEDC WIND TUNNEL TEST CONDITIONS .....	1
TABLE 2 PROGRAM INPUT DATA .....	8
TABLE 3 TRANSITION FREQUENCIES AND REYNOLDS NUMBERS .....	9

## NOMENCLATURE

$A$	Amplitude function, two dimensional disturbance $\{  q(y)  e^{-\alpha_{\delta_i} x} \}$ Initial amplitude of the disturbance introduced into the boundary layer.
$\alpha_{\delta}$	Non-dimensional disturbance wave number in the streamwise direction $\left( \frac{2\pi\delta}{\lambda_x} \right)$
$\beta$	Non-dimensional disturbance wave number in the spanwise direction $\left( \frac{2\pi\delta}{\lambda_z} \right)$
$c$	Non-dimensional disturbance phase velocity. complex quantity $(c_r + ic_i)$
$\frac{dA}{dx}$	Spatial amplification rate $(-\alpha_{\delta_i} A)$
$\delta$	Boundary layer thickness
$f$	Perturbation dimensional frequency [kHz] Maximum amplified frequency at the transition Reynolds number [kHz]
$F$	Perturbation non-dimensional frequency
$m(y)$	Mass flux eigenfunction. Complex function $(m_r(y) + im_i(y))$
$m'(x, y, t)$	mass fluctuation function
$M$	Freestream Mach number
$N(f)$	N-Factor, function of frequency
$\eta$	Eigenfunction phase angle $\left\{ \tan^{-1} \left( \frac{q_r(y)}{q_i(y)} \right) \right\}$
$p(y)$	Pressure eigenfunction. Complex function $(p_r(y) + ip_i(y))$
$p'(x, y, t)$	Pressure fluctuation function
$q'(x, y, z, t)$	General disturbance function $(Ae^{i\theta})$
$q(y)$	General eigenfunction. Complex function $(q_r(y) + iq_i(y))$
$\Psi$	Wave propagation angle $\left\{ \tan^{-1} \left( \frac{\beta}{\alpha} \right) \right\}$
$Re_x$	Reynolds number based on freestream direction $x$
$R$	Square root of Reynolds number based on freestream direction $x$ $(\sqrt{Re_x})$
$T$	Freestream Total Temperature [ $^{\circ}R$ ] Wall Temperature degrees Rankine [ $^{\circ}R$ ]
$T(y)$	Temperature eigenfunction. Complex function $(T_r(y) + iT_i(y))$
$T(x, y, t)$	Temperature fluctuation function
$t$	Time [sec]
$u(y)$	$u$ velocity eigenfunction. Complex function $(u_r(y) + iu_i(y))$
$v(y)$	$v$ velocity eigenfunction. Complex function $(v_r(y) + iv_i(y))$
$\omega$	Non-dimensional frequency. Complex function $(\alpha c)$
$x$	Freestream spatial direction

Y	Surface normal direction. non-dimensional
$\theta$	Phase of the general disturbance $\{ [\alpha_{\delta r} x + \beta_{\delta r} z] + [\alpha_{\delta i} c_i - \alpha_{\delta r} c_r] * t + \eta \}$
<u>Subscripts</u>	
w, wall	Wall conditions
$\infty$	Freestream
e	Boundary Layer edge
o	Freestream Total conditions, initial condition ( $A_o$ )
r	Real part of eigenfunction
i	Imaginary part of eigenfunction

## 1.0 INTRODUCTION

Results of experimental investigations of stability characteristics of hypersonic laminar boundary layers on planar and conical (sharp and blunt-nosed) models (Ref.1) indicated that stability theory can form a useful basis for describing and interpreting wind tunnel data. The results of (Ref.1) indicate that the measured boundary layer stability characteristics of simple configurations were described well in a general sense by boundary layer stability theory. Measurements showed well-defined disturbances in the laminar boundary layer which amplified until breaking down into turbulence. Although linear stability theory was only partially successful in predicting the amplification rate of these disturbances, their frequency range and phase velocity was predicted well by linear stability theory. Although the transition Reynolds numbers measured in conventional wind tunnels are generally lower than in free flight (Ref.2), the results of Stetson and Kimmel indicate that the stability process in a hypersonic facility like AEDC VKF Tunnel B is similar to the presumed free-flight stability mechanism. The ambient wind tunnel noise tends to be at lower frequencies than the dominant boundary layer instability, and the interaction between them is very limited (Ref.1., Ref.3). The lower wind tunnel transition Reynolds number thus results, presumably, from larger, but still linear initial disturbance amplitudes.

The supposition that boundary layer stability in a wind tunnel environment can be described by linear stability theory for simple configurations (at least) opens the possibility of using linear stability theory for transition prediction and design of wind tunnel models. An additional implication is that wind tunnel transition results may be related to flight transition results by using linear stability theory. Transition in a wind tunnel might, in effect, be "calibrated" for a limited range of models and conditions.

The stability of the laminar boundary layer on a sharp, 7-degree half angle cone with freestream Mach numbers of 6.0 and 8.0 was numerically investigated using the linear stability code e-Malik (Ref.4). Four cases were studied, each of which modeled wind tunnel conditions from tests performed at the AEDC Von Karman Hypersonic Tunnel B. The cases studied were:

**Table 1 AEDC Wind Tunnel Test Conditions**

CASE #	$M_\infty$	$T_o$ [R]	$T_{wall}/T_o$
1	8.0	1310.00	Adiabatic
2	8.0	1310.00	0.41
3	6.0	1049.67	0.63
4	6.0	1310.00	0.41

Hot-wire anemometer measurements were used to determine the most amplified frequency at transition. The comparison of measured and computed most-amplified frequency provides an indication of how well experimental stability processes were described by linear stability theory. Linear stability theory was used to compute an N-factor to predict transition for each of the cases. The N-factor, described in Section 4, is a correlating parameter which, when measured for one case, may be used to predict transition for other cases. Case 1 provided a baseline N-factor

which was then used to predict transition for the other cases. Cases 2, 3, and 4 provided an assessment of wall cooling effects, and cases 2 and 4 provided an assessment of Mach number effects.

## 2.0 Experimental Configuration

The experimental cases are documented in Refs. (5, 6, 7) and summarized in Table 1. Boundary layer stability data were obtained using hot-wire anemometers for cases 1, 2, and 4. In addition, heat transfer measurements were used to obtain the mean transition location for the cold-wall cases (2, 3 and 4). Transition is determined from heat transfer measurements by noting where heat transfer rates first rise above laminar values. Transition was measured using hot-wire anemometry for the adiabatic wall case 1 by noting where disturbance levels had maximized and begun to decay. Previous comparisons of hotwire to heat transfer measurements indicate a good correlation between transition locations measured with these two techniques (Ref. 8). Figure A1 shows the experimental setup (hotwire probe and sharp cone) at AEDC Tunnel B.

In supersonic flow the hot-wire responds to fluctuations of mass flux and total temperature (the sensing variables) whereas the fluctuations which characterize an unsteady flowfield are those of vorticity, entropy and sound (the independent mode variables). Fluctuations in the sensing and mode variables are inferred from hot-wire a-c voltage response (rms.) measurements using modal analysis. For detailed information on modal analysis refer to (Ref. 1,12).

At each model station the hot-wire probe was traversed across the boundary layer to locate the point of maximum rms voltage output of the wire (See figure A2). The quantitative hot-wire data were acquired at these maximum energy points at each of the profile survey stations. The recorded signals were processed using the spectrum analyzer followed by application of computer routines to eliminate the electronic noise and to restore the spectrum of the wire response data. The results were a "noise-free", restored amplitude-squared spectral density distribution  $A^2(f)$  over an effective frequency range from zero to 600 [kHz] (See figures A3, A4).



### 3.0 COMPUTER CODE e - Malik

This computer program (Ref.4) solves the Stability Equations using Spatial Theory (amplitude of the disturbance changes with respect to space not time). The disturbance wave number ( $\beta$ ) in the spanwise direction and the frequency ( $\omega$ ) are prescribed as real quantities. The numerical problem is to obtain the eigenvalue ( $\alpha$ ). This is a complex quantity indicating the wave number in the streamwise direction. This program allows the user to perform linear stability analysis for 2D and axisymmetric flows for sharp and blunt bodies. It also allows for the computation of eigenfunctions  $\{u(y), v(y), p(y), T(y)\}$  and for the computation of N-Factor curves for specified frequencies. Section 3.0 describes the relation between eigenvalues, eigenfunctions and N-Factors.

#### 4.0 SPATIAL THEORY

The general disturbance in a boundary layer  $q'(x, y, z, t)$  is represented as:

$$q'(x, y, z, t) = q(y) * \exp[i(\alpha_\delta x + \beta_\delta z - \alpha_\delta c t)]$$

where the non-dimensional wave number in the freestream (x) direction is:

$$\alpha_\delta = \alpha_{\delta r} + i\alpha_{\delta i}$$

the non-dimensional wave number in the spanwise z-direction is:

$$\beta_\delta = \beta_{\delta r} + i\beta_{\delta i}$$

the disturbance phase velocity is:

$$c = c_r + ic_i$$

Substituting the expressions for  $\alpha, \beta, c$  into the disturbance function we obtain (after some algebraic manipulations), the following:

$$q'(x, y, z, t) = q(y) * \exp[(\alpha_{\delta r} c_i + \alpha_{\delta i} c_r) * t - (\alpha_{\delta i} x + \beta_{\delta i} z) + i(\alpha_{\delta r} x + \beta_{\delta r} z + t * [\alpha_{\delta i} c_i - \alpha_{\delta r} c_r])]$$

The eigenfunction is given as,

$$q(y) = [q_r(y) + iq_i(y)]$$

$$q(y) = |q(y)| e^{i\eta}$$

where  $\eta = \tan^{-1}\left(\frac{q_i(y)}{q_r(y)}\right)$  is the eigenfunction phase angle ; therefore

$$q(y) = |q(y)| * [\cos(\eta) + i \sin(\eta)]$$

Observing the amplitude function, for a given time  $t$ , the amplitude of the disturbance is constant along the line  $\alpha_{\delta i}x + \beta_{\delta i}z = \text{const}$ , this is a line of constant phase in the  $x$ - $z$  plane. This constant phase line advances with a phase velocity  $c_{ph} = \frac{\omega_{\delta}}{\alpha_{\delta}}$ .

When  $\beta_{\delta} = 0$ , the direction of propagation of the wave is in the freestream or  $x$  direction. If  $\beta_{\delta} \neq 0$ , the wave propagation direction is inclined at an angle  $\psi$  with respect to the freestream  $x$  direction. The wave propagation direction is always normal to the constant phase line in the  $x$ - $z$  plane. The angle is given by:  $\psi = \tan^{-1}\left(\frac{\beta_{\delta}}{\alpha_{\delta}}\right)$ . Even if the boundary layer basic state is two

dimensional, oblique disturbances are three dimensional.

For the spatial theory development (Ref.9), time dependency is eliminated, therefore the amplitude function becomes:

$$A = |q(y)| \exp[-(\alpha_{\delta i}x + \beta_{\delta i}z)]$$

For a two dimensional disturbance (amplitude only changes in the  $x$  - direction),  $\beta_{\delta i} = 0$  therefore the amplitude function becomes:

$$A = |q(y)| \exp[-(\alpha_{\delta i}x)]$$

The change in amplitude with respect to  $x$  variable is known as the spatial amplification rate and is given by the following equation :

$$\frac{dA}{dx} = (-\alpha_{\delta i}) |q(y)| \exp[-\alpha_{\delta i}x]$$

But  $A = |q(y)| \exp[-(\alpha_{\delta i}x)]$  is the original amplitude function, therefore,

$$\frac{dA}{dx} = -\alpha_{\delta i} A, \text{ where } (-\alpha_{\delta i}) \text{ is known as the amplification factor.}$$

The N-Factor is defined as follows :

$$\frac{d}{dx} \ln A = \left( \frac{1}{A} \frac{dA}{dx} \right) = -\alpha_{\delta i}$$

$$N(f) = -\int_{x_0}^x \alpha_{\delta i} dx$$

$$\frac{A}{A_0} = e^{N(f)} ; \text{ where } A_0 \text{ is the initial amplitude of the disturbance at the lower neutral bound where}$$

the disturbance first begins to amplify.

The N-Factor is a measure of how much a particular disturbance amplitude grows as it travels downstream relative to its initial amplitude. For this study, it was computed for each specific frequency for a range of Reynolds numbers. The computation was repeated for various frequencies until the most amplified frequency was obtained at the transition Reynolds number.

Much work has shown that an N-factor of 9 may be correlated with transition in a variety of free-flight conditions (Ref. 11). This correlation pre-supposes many conditions, such as the

freestream disturbance levels being of equal magnitude for all conditions, and that non-linear effects prior to transition are equal for all cases, and may be lumped in with the linear instability. Despite these assumptions, the  $e^N$  method has been useful in rationally taking parameter variations into account in transition prediction. The fundamental step in using  $e^N$  in non-freeflight conditions is obtaining a value of  $N$  which correlates transition. Assuming transition occurs at a constant terminal disturbance level  $A$ , the  $N$ -value will be lower in the wind tunnel environment since the initial  $A_0$  value will be higher. In this study, Case 1 was used to determine the  $N$ -factor for AEDC Tunnel B. This  $N$ -factor was then used to predict transition on cases 2, 3, and 4.

Another concept that needs to be introduced is the subject of normal modes of oscillation (1<sup>st</sup>, 2<sup>nd</sup>, ...,etc.). Normal modes are easier to visualize in the case of solid media. The normal modes of the boundary layer are exactly analogous. A cantilever beam system will be used to demonstrate this concept. In general, if a sinusoidal excitation is applied to a beam at a resonant frequency (this system has more than one resonant frequency) also referred to as a normal mode frequency, and then removed, the instantaneous deflection of the beam is referred to as the normal mode shape. The eigenfunctions obtained for this problem give the normal mode shapes. Like the cantilever beam, the boundary layer is an oscillator with resonance's. Instability waves correspond to normal modes of the boundary layer and although they are more difficult to identify from calculations and measurements than in solid mechanical systems, they consist of well defined disturbances with particular mode shapes, or eigenfunctions and specific combinations of phase velocity and frequency.

When the mean flow relative to the disturbance phase velocity ( $c_s$ ) is supersonic over some portion of the boundary layer mean velocity profile, there are an infinite number of wave numbers ( $\alpha$ ) (solutions of the eigenvalue problem) for a single phase velocity. These additional disturbances are called higher modes (Mack, ref. 9). Freestream Mach number and wall cooling dictates which mode of oscillation will dominate. For subsonic flow the amplification rates are higher for first mode type oscillations, for supersonic flow the amplification rates are higher for second mode type oscillations.

## 5.0 NUMERICAL COMPUTATIONS

Program e-Malik was used to obtain amplification rates, N-Factor curves and eigenfunctions for specified frequencies. The input conditions to the code matched the various wind tunnel conditions used in tests performed at AEDC Tunnel B. These results were later used to compute perturbation contours of  $\{p'(x, y, t), T'(x, y, t), m'(x, y, t)\}$ .

The inputs to the program for each test case are listed in Table 1.

**Table 2 Program Input Data**

CASE #	$M_\infty$	$M_{\text{edge}}$	$T_o$ [R]	$T_{\text{wall}}/T_o$	$Re_x$ [ft] <sup>-1</sup>
1	8.0	6.8	1310.00	Adiabatic	1.0e06
2	8.0	6.8	1310.00	0.41	1.0e06
3	6.0	5.2	1049.67	0.63	1.0e06
4	6.0	5.2	1310.00	0.41	1.0e06

For the computation of the perturbation contours, program e-Malik was used to compute the eigenfunctions at the transition location. This location was obtained during the wind tunnel tests by using heat transfer and hot-wire measurements for each of the cases studied. The perturbation contours were obtained by expanding the eigenfunctions in the streamwise direction using the following equation,

$$q'(R, y, t = 0) = |q(y)| * e^N * \cos[\alpha_{\delta_r} * R + \eta]$$

## 6.0 GENERAL RESULTS

Measured (where available) and computed values of most-amplified frequency and transition Reynolds number are summarized in Table 3. These computations are based on 2-D disturbances only. This is justified since 2-D second mode disturbances have the highest amplified rates at these Mach numbers (Ref. 8).

**Table 3 Transition frequencies and Reynolds numbers**

Case #	$T_w/T_o$	Measured $Re_x$	Predicted $Re_x$	Measured $f_{max}$ [kHz]	Predicted $f_{max}$ [kHz]
1	adiabatic	$4.7 \times 10^6$	base line	90	90
2	0.41	$3.2 \times 10^6$	$3.2 \times 10^6$	110	120
3	0.63	$3.36 \times 10^6$	$3.96 \times 10^6$	125	100
4	0.41	$3.47 \times 10^6$	$2.9 \times 10^6$	not available	145

A comparison of measured transition Reynolds number to computed N-factors for Case 1 indicated a transition N-factor of 4.4 for AEDC VKF-B. This N-factor value was then used to predict transition for the other three cases. Figures A5, A6, A7 and A8 show the computed N-factor curves for various frequencies.

In general, the maximum amplified frequency ( $f_{max}$ ) at transition was predicted well by the  $e^N$  method. Stetson and Kimmel (Ref.1) have shown that the maximum amplified frequency is equal to approximately  $0.5U_e / \delta$  for a number of cases. This is because typically, the second mode wavelength is approximately  $2\delta$ , and its convection velocity is nearly equal to  $U_e$  (Ref.9).

The predicted transition Reynolds number for the cold wall Mach 8 (case 2) agrees well with the measured value. This indicates that the basic stability mechanism and the wall temperature effects on it are described well by linear stability theory. Although linear stability theory was inaccurate in predicting the disturbance amplification rates for Case 1 (Ref.10), the good agreement between the predicted and measured cold wall transition Reynolds numbers in Case 2 indicates that any errors must be consistent between the two cases (1 & 2). Linear stability theory predicts a destabilizing effect of reduced wall temperature ratio, with increasing second mode amplification rates. Also, the maximum amplified frequency increases due to the decrease in boundary layer thickness with wall cooling, this is observed when comparing Cases 1 and 2.

The transition Reynolds number for Case 3 was overpredicted by the  $e^N$  method by 18%, although the trend of lower transition Reynolds number compared to Case 1 is accurately replicated. Mack (Ref. 8) shows that, for 2D mean flows, second mode amplification rates begin to dominate at  $M > 4.0$ . Mack's description is for general 2D mean flow. He also shows that as freestream Mach number increases, the boundary layer becomes more stable, (transition Reynolds number increases). When comparing Case 3 to Case 1, since they both dominated by second

mode waves, a lower transition Reynolds number is to be expected for Case 3, since both wall cooling and decreased Mach number destabilize the second mode boundary layer.

Case 4 is identical to Case 3, except that the stagnation temperature is increased and the wall cooling is increased, to produce a ratio of  $(T_w / T_o)$  of 0.41. The transition Reynolds number was underpredicted by 20%. The  $e^N$  method predicts a transition Reynolds number of  $2.9 \times 10^6$ , about 73% of the predicted Case 3 transition Reynolds number. Several competing effects combine to create this lower predicted transition Reynolds number. First, the increased wall cooling destabilizes the second mode, but stabilizes the first mode. Since second mode disturbances first begin to amplify as first mode, this would have an effect on the maximum amplitude which a disturbance reaches. Since the second mode growth rates are much higher than the first, however, the effect of wall cooling on the second mode would be expected to dominate the effect of wall cooling on the first mode. Second, increased stagnation temperature stabilizes the boundary layer (Ref.12). The measured transition Reynolds number, however, is almost identical to Case 3. A measured maximum amplified frequency is not available for this case, but the computed maximum amplified frequency was 145 kHz. This is significantly higher than any of the other cases examined. This high frequency is due to the combination of a thinner boundary layer, due to the increased wall cooling, and a higher edge velocity, due to the increased stagnation temperature. This high frequency indicates that perhaps a third effect is coming into play which is not accounted for in this application of the  $e^N$  method. Previous measurements of the ambient wind tunnel noise in this facility (Ref.1) indicated that the amplitude of freestream disturbances drops off with increasing frequency, roughly proportional to  $1 / f$ . When the predicted maximum amplified frequency becomes sufficiently different from the baseline case used to determine an N-factor, the initial  $A_o$  used to describe the N-factor changes. In this case, since the predicted most-amplified frequency is much higher than the most-amplified frequency of the baseline case, the initial  $A_o$  amplitude is lower, leading to a higher N-factor at transition, assuming that  $A(\text{transition})$  is identical for all cases. It would, perhaps, be appropriate to take this into account in future transition predictions.

Figure A1 shows the AEDC Tunnel B Experimental Setup. 7-degree sharp angle cone and single hot-wire assembly.

Figure A2 shows the hot-wire anemometer peak fluctuation energy signal located at a height of 85-90% of the boundary layer thickness ( $\delta$ ) for  $M_\infty=8.0$  flow. Hot-wire sensitivity coefficients are a function of the mean flow. If the hot-wire is always positioned at a location where the mean flow is the same, then the sensitivity coefficients do not change. For similar boundary-layer profiles (e.g. sharp cone) if the wire is placed at the same  $y/\delta$  position in the boundary layer, as the x station along the model is varied, disturbance amplification rates may then be obtained directly from the hot-wire rms signals.

Figure A3 shows Fluctuation spectra at the location of peak energy in the boundary layer at approximately  $0.9\delta$  for adiabatic,  $M_\infty=8.0$ , sharp cone flow. Second mode disturbances grow much faster than first mode disturbances and rapidly become the dominant mode.

Figure A4 contains the same data as figure A3 with spectral data from several stations overlaid to better illustrate the disturbance frequencies. The first and second mode fluctuation frequency bands are merged.

Figures A5 through A8 show the computed N-Factor curves. Case #1 was used as the baseline for obtaining an N-Factor for AEDC Tunnel B. The measured transition Reynolds number was  $4.7 \times 10^6$ , the corresponding transition N-Factor value obtained from figure 1 is 4.4. As stated before,  $A/A_0 = e^N$ , therefore,  $A/A_0 = e^{4.4} = 81.45$ . The amplitude of an initial disturbance has increased 81.45 times its initial amplitude (at the lower neutral stability curve) by the time it reaches transition. This value of  $N = 4.4$  was used to obtain the transition location for the remaining cases from figures A6, A7 and A8.

Figures A9 through A20 show the computed magnitude of the eigenfunctions. The general disturbance can be expressed as :

$$q' = Ae^{i\theta} = A[\cos(\theta) + i \sin(\theta)]$$

$$A = |q(y)|e^{-\alpha_i x}$$

$$\theta = [\alpha_i x] \leftarrow \text{phase angle}$$

The magnitude of the eigenfunction is contained in the amplitude function of the disturbance. All quantities (pressure, temperature, mass) are described by this equation. For a specific case, the magnitudes between the quantities are different but the amplification rate is the same. The shapes of the eigenfunctions indicate where the strongest signals are going to be located across the boundary layer. For hotwire measurements we are mostly interested in the massflux eigenfunction (hotwires are sensitive to massflux and total temperature). Figures A17 through A20, show a maximum away from the wall close to the boundary layer edge. This is why the strongest signals are measured near the boundary layer edge.

Figures A21 through A32 show the computed eigenfunction phase angle. The eigenfunctions are a complex quantities. The general representation is :

$$q(y) = q_r(y) + iq_i(y)$$

The eigenfunction phase angle is given by :

$$\eta = \tan^{-1} \left( \frac{q_i(y)}{q_r(y)} \right)$$

This angle is contained in the general 2D-disturbance equation given as :

$$q'(x, y, t) = |q(y)|e^{-\alpha_i x} \cos(\alpha_i x + \eta)$$

$\eta$  represents a phase shift in the general cosine function. Pressure, temperature and massflux phase shifts are different since the eigenfunctions are different. The phase shift would be measured in a wind tunnel experiment by placing two hot-wire probes, one above the other in the boundary layer, and measuring the time delaying the signal between the two probes.

Figures A33 through A44 show the 2D contours of the real part of the eigenfunction. These plots show how the fluctuations begin to amplify as they travel downstream. The N-Factor computation indicate the rate of amplification of the disturbances. The equation describing these plots is :



$$q'(R, y, t = 0) = |q(y)|e^N \cos(\alpha, R + \eta)$$

These contours are generated for a single frequency. The frequency chosen for each case was the maximum predicted frequency (Table 1). The N-curves used are the ones computed for each maximum predicted frequency, a different curve for each case study.

Figures A45 through A48 show show the 3D representation of the real part of the mass eigenfunction. The equation used to generate them is the same as the one used to generate figure A37 through A40. The most amplified frequency for each case is represented.

Figures A49 through A52 show the real part of the mass eigenfunction at a constant y location. The equation used to generate them is the same as the one used to generate figure A41 - A44. The y location chosen is where the magnitude of the eigenfunction curve shows a maximum. See figures A17 through A20.

## 7.0 CONCLUSIONS

The comparison study between cases 1 and 2 and between cases 3 and 4 showed that the stability parameters are very sensitive to the ratio of  $(T_w / T_o)$ . The smaller ratio of  $(T_w / T_o)$  resulted in a decrease in the predicted transition Reynolds number. This indicates that wall cooling destabilizes second mode waves by increasing their amplification rate and causing transition to occur more rapidly (Cases 3 and 4).

Freestream Mach number dictates what mode (first, second) will be amplified the most, once the dominant mode is established, amplification rates of particular frequencies become sensitive to thermal conditions, specifically to the ratio of  $(T_w / T_o)$ .

Linear stability theory properly described the processes leading towards transition at AEDC Tunnel B by matching ( Case 1) or coming close to matching the predicted maximum amplified frequency with the measured frequencies. This indicates that AEDC Tunnel B can be used to conduct stability tests and produce reliable test data with the use of transition N-Factor correlation's for given geometry's and test conditions.

## 8.0 REFERENCES

1. Stetson, K. F., and Kimmel, R. L., "On Hypersonic Boundary-Layer Stability," AIAA paper 92-0737, 1992.
2. Beckwith, I. E., "Development of a High Reynolds Number Quiet Tunnel for Transition Research," AIAA J., vol. 13, no. 3, pp. 300-306.
3. Kimmel, R. L., and Kendall, J. M., "Nonlinear Disturbances In a Hypersonic Laminar Boundary Layer," AIAA paper 91-0320, 1991.
4. Malik, Mujeeb R., " $e^{\text{Malik}}$ : A New Spatial Stability Analysis Program for Transition Prediction Using the  $e^N$  Method", High Technology Report No. HTC-8902, March 1989
5. Stetson, Kenneth F., Thompson, Elton R., Donaldson, Joseph C., and Siler, Leo G., "Laminar Boundary Layer Stability Experiments on a Cone at Mach 8, Part 5: Tests with a Cooled Model", AIAA Paper No. 89-1895, AIAA 20th Fluid Dynamics, Plasma Dynamics and Lasers Conference, Buffalo, New York, June 12-14, 1989
6. Stetson, Kenneth F., Thompson, Elton R., Donaldson, Joseph C., and Siler, Leo G., "Laminar Boundary Layer Stability Experiments on a Cone at Mach 8, Part 1: Sharp Cone", AIAA Paper No. 83-1761, AIAA 16th Fluid and Plasma Dynamics Conference, Danvers, Massachusetts, July 12-14, 1983
7. Kimmel, R. L., "Experimental Transition Zone Lengths in Pressure Gradient in Hypersonic Flow," Transitional and Turbulent Compressible Flows, ASME FED vol. 151, L. D. Kral and T. A. Zang eds., 1993, pp. 117-127.
8. Mack, L.M., "Boundary Layer Stability Theory", Rep. 900-277 Rev. A, Nov 1969, Jet Propulsion Lab., Pasadena, California
9. Chen, F. J., Malik, M. R., and Beckwith, I. E., "Comparison of Boundary Layer Transition on a Cone and Flat Plate at Mach 3.5," AIAA J., vol. 27, no.6, pp. 687-692, June 1989.
10. Mack, L. M., "Boundary Layer Stability Analysis For Sharp Cones at Zero Angle-of-Attack," Air Force Wright Aeronautical Laboratories, AFWAL-TR-86-3022, August 1986.

11. Morkovin, M.V., "Fluctuations and Hot-wire Anemometry in Compressible Flows",  
AGARDograph 24, November 1956.

## APPENDIX A

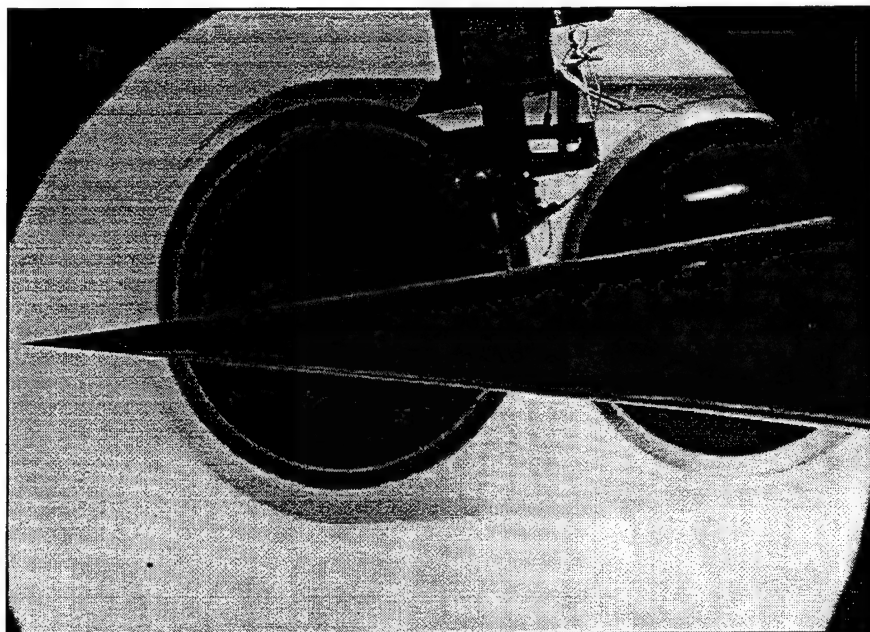


Figure A 1 Experimental Setup AEDC Tunnel B

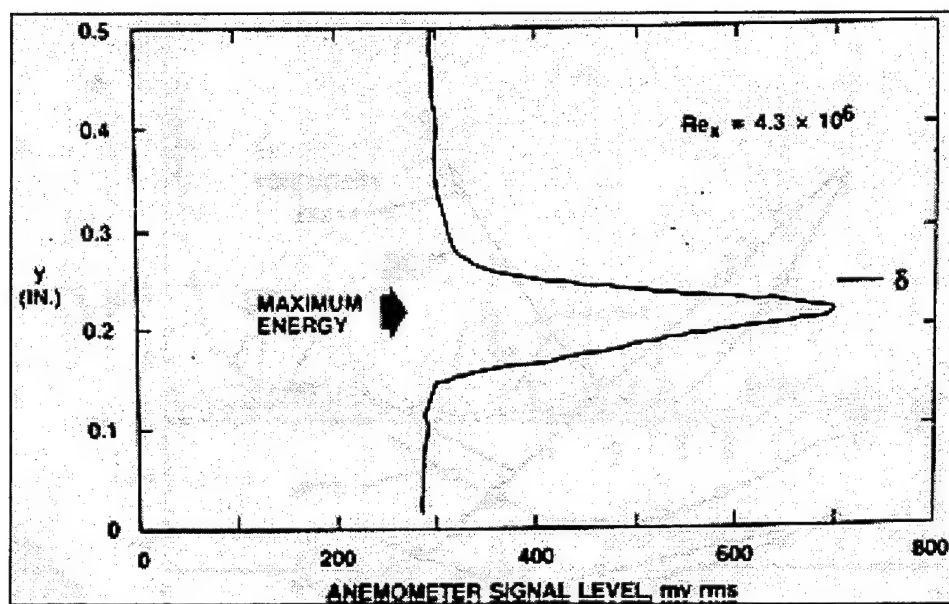


Figure A 2 Hot-wire anemometer profile

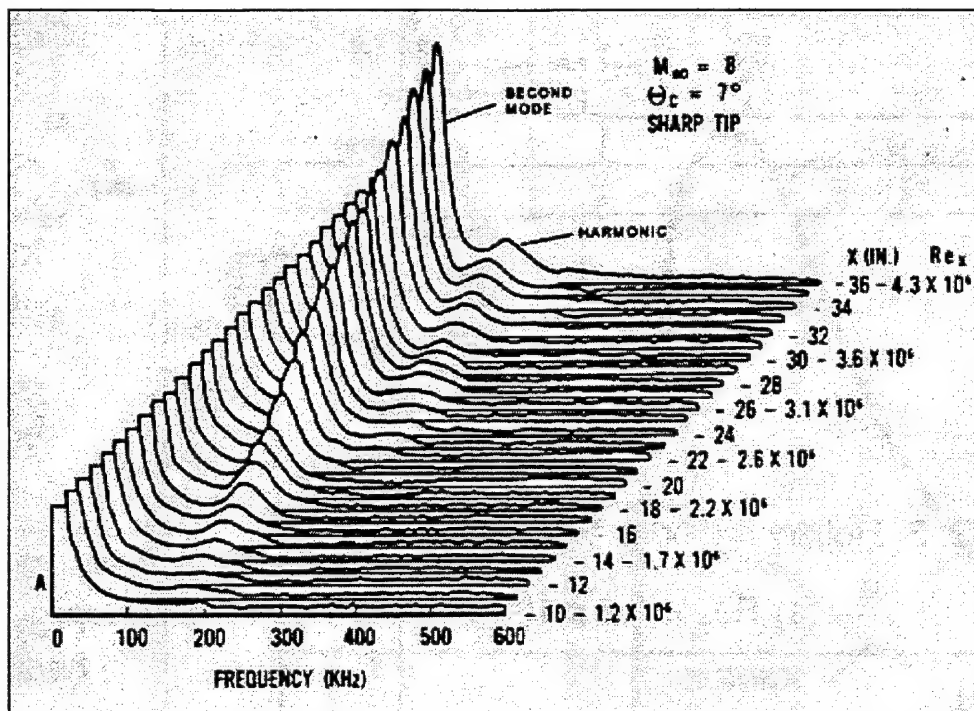


Figure A 3 Boundary layer fluctuation spectra

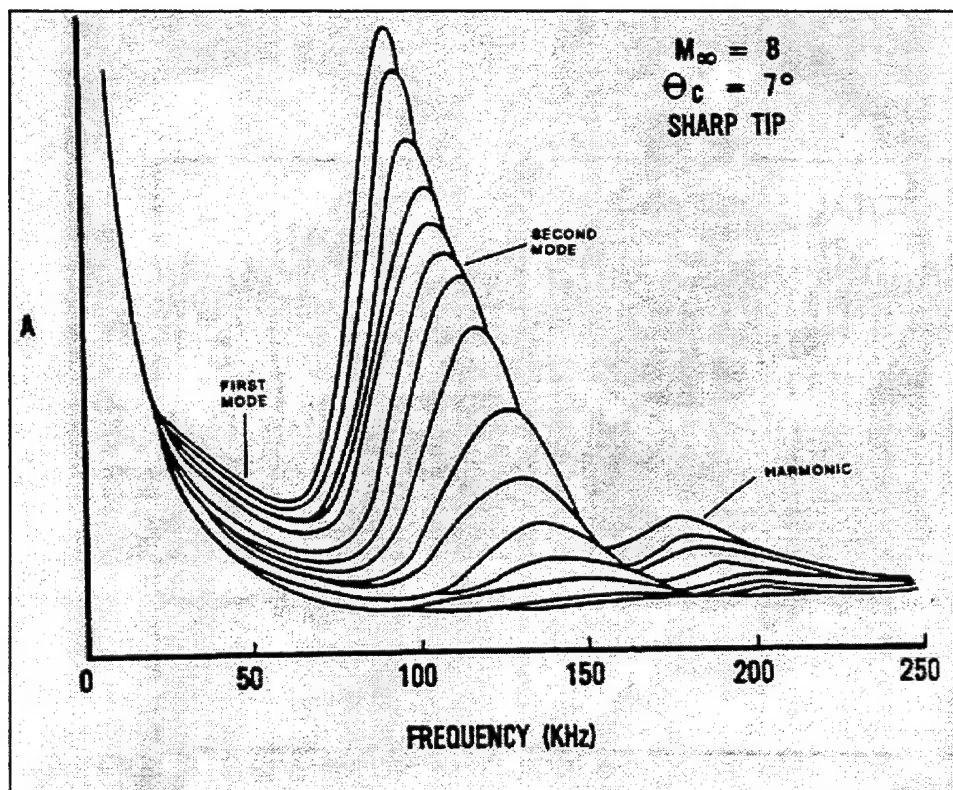


Figure A 4 Fluctuation spectra overlaid

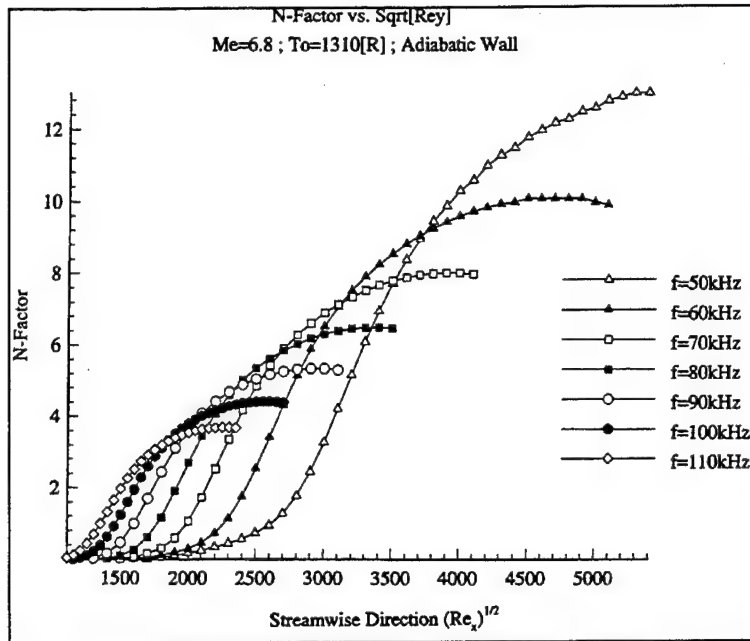


Figure A 5 N-Factor Curves, M=8.0, Adiabatic

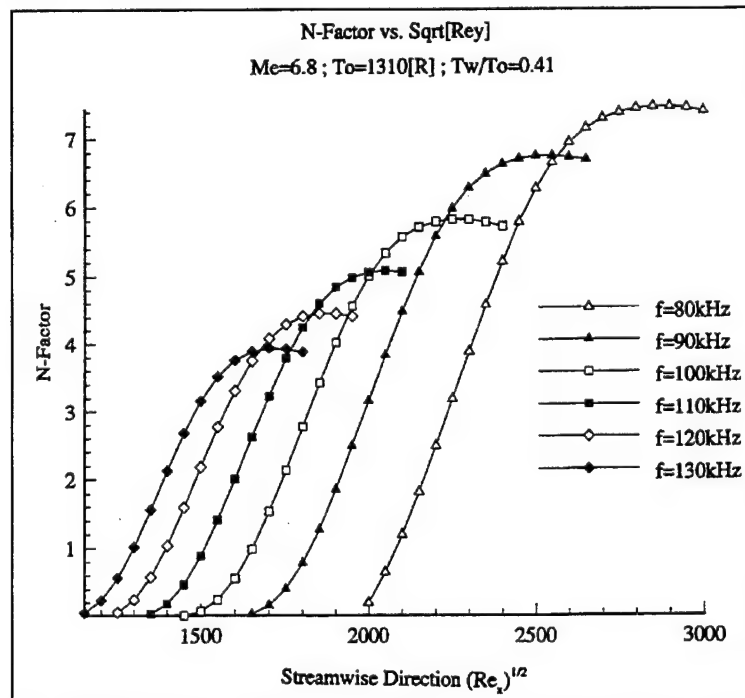
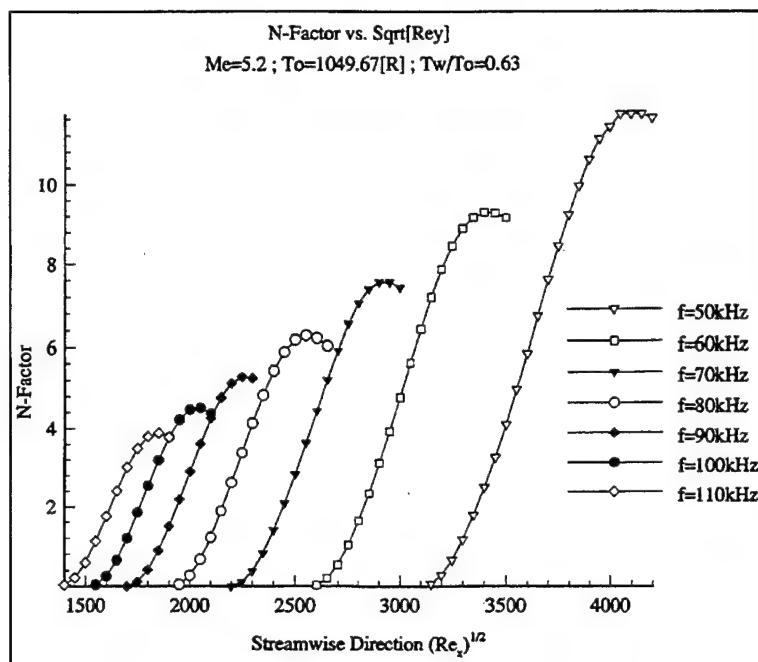
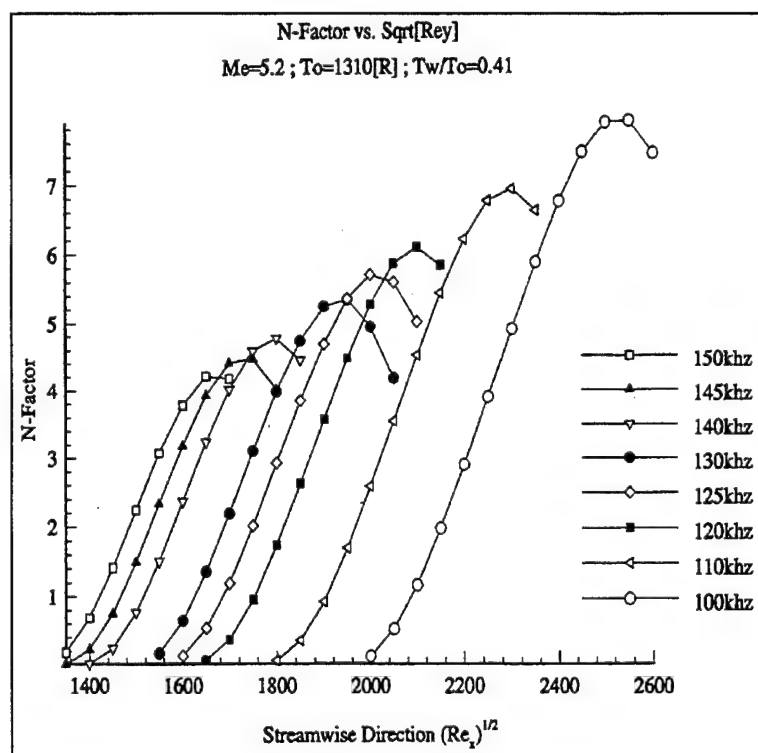


Figure A 6 N-Factor Curves, M=8.0, Tw/To=0.41



**Figure A 7 N-Factor Curves,  $M=6.0$ ,  $Tw/To=0.63$**



**Figure A 8 N-Factor Curves,  $M=6.0$ ,  $Tw/To=0.41$**



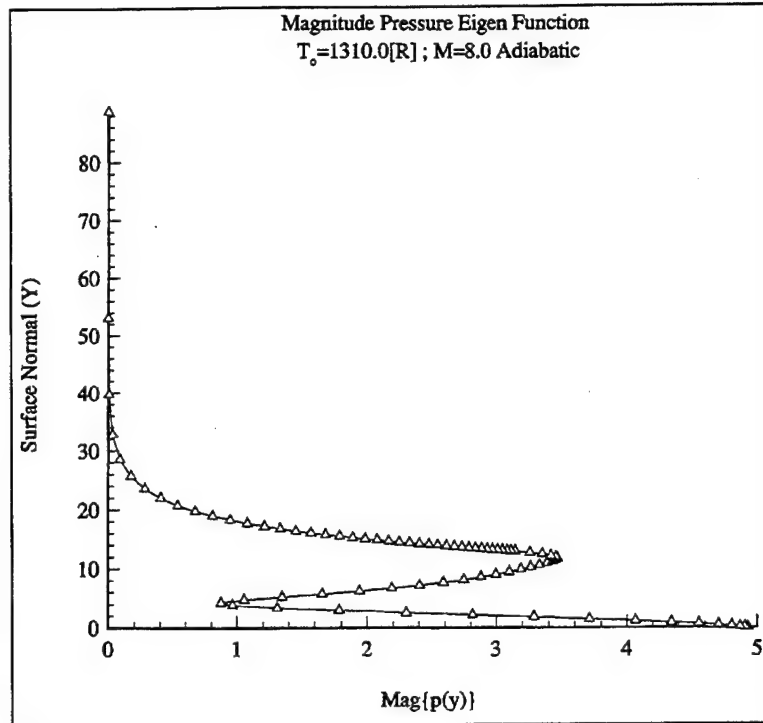


**Figure A 9 Mag. Pressure eigenfunction,  $M=8.0$ , Adiabatic**

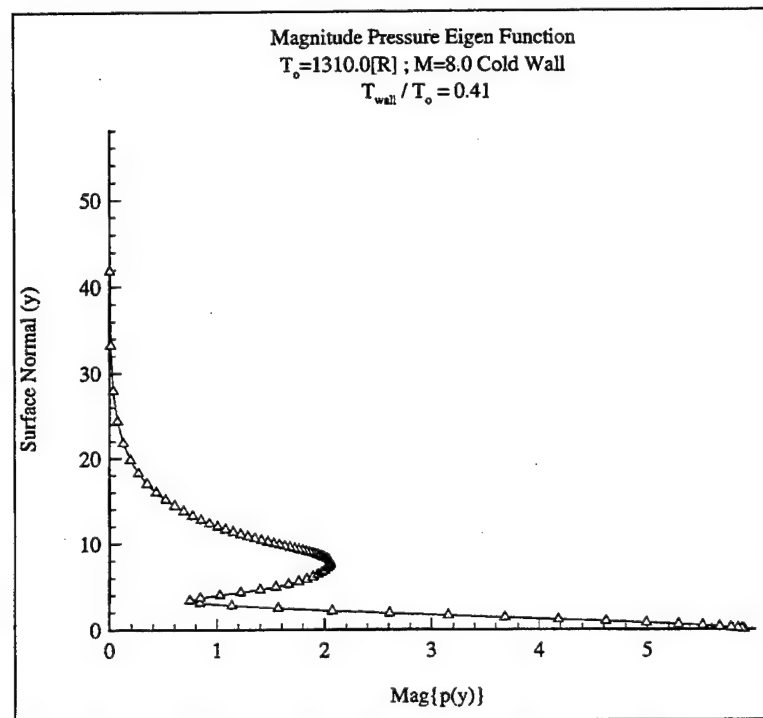


**Figure A 10 Mag. Pressure eigenfunction,  $M=8.0$ ,  $T_w/T_o=0.41$**

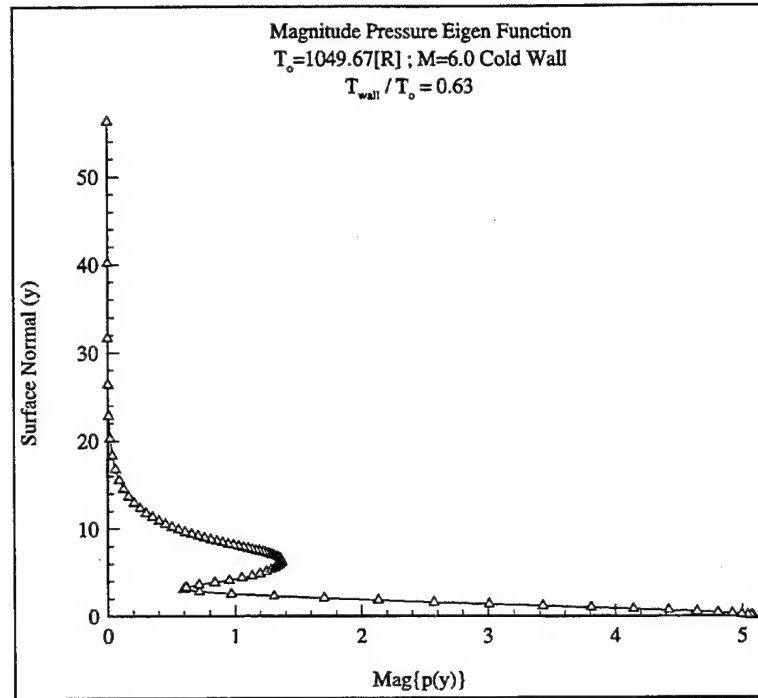


**Figure A 11 Mag. Pressure eigenfunction,  $M=6.0$ ,  $T_w/T_o=0.63$**

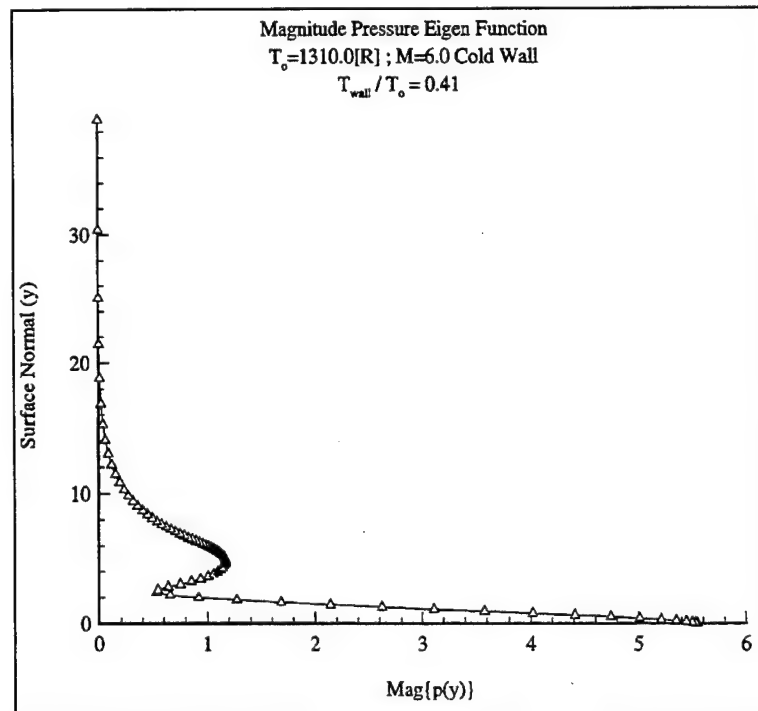


**Figure A 12 Mag. Pressure eigenfunction,  $M=6.0$ ,  $T_w/T_o=0.41$**

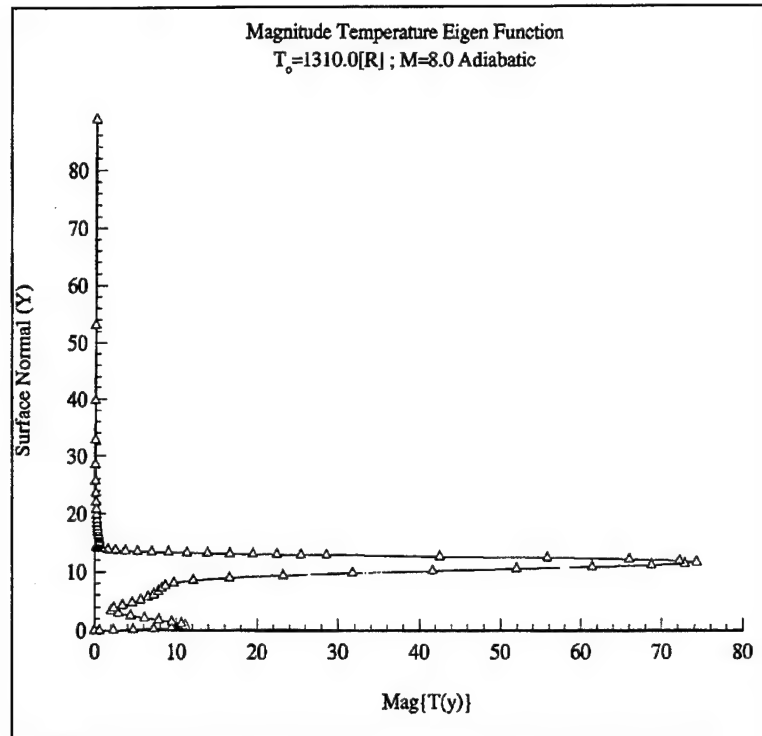


Figure A 13 Temperature eigenfunction,  $M=8.0$ , Adiabatic

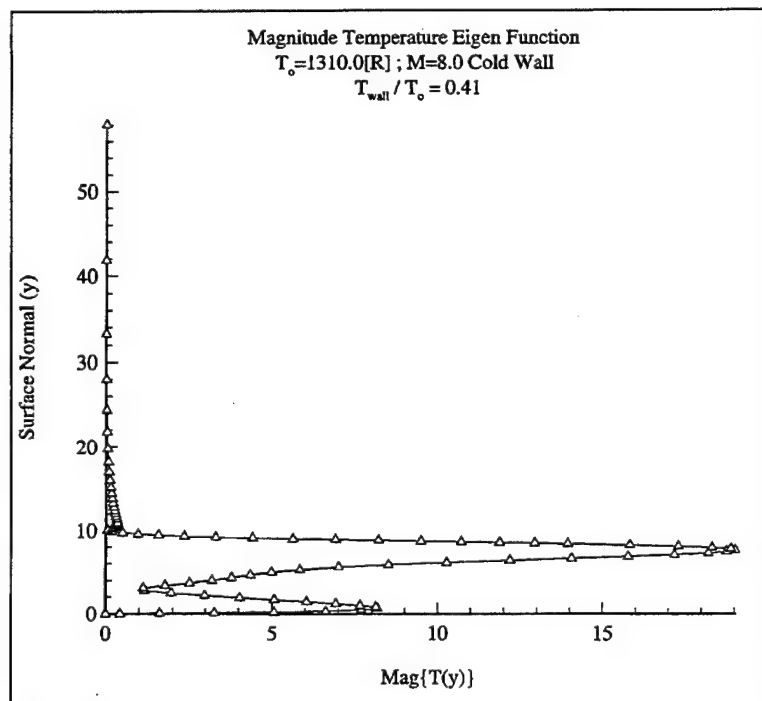
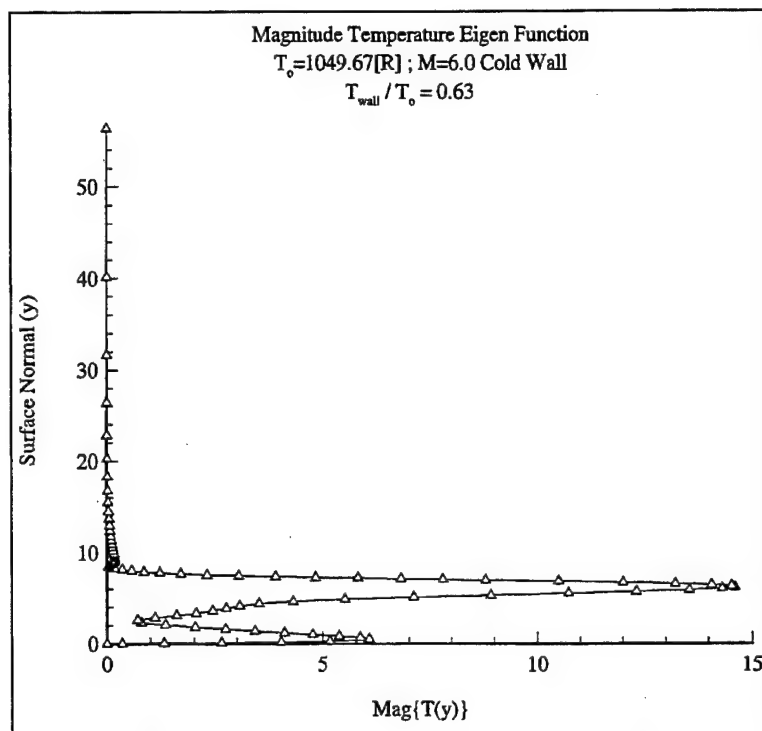
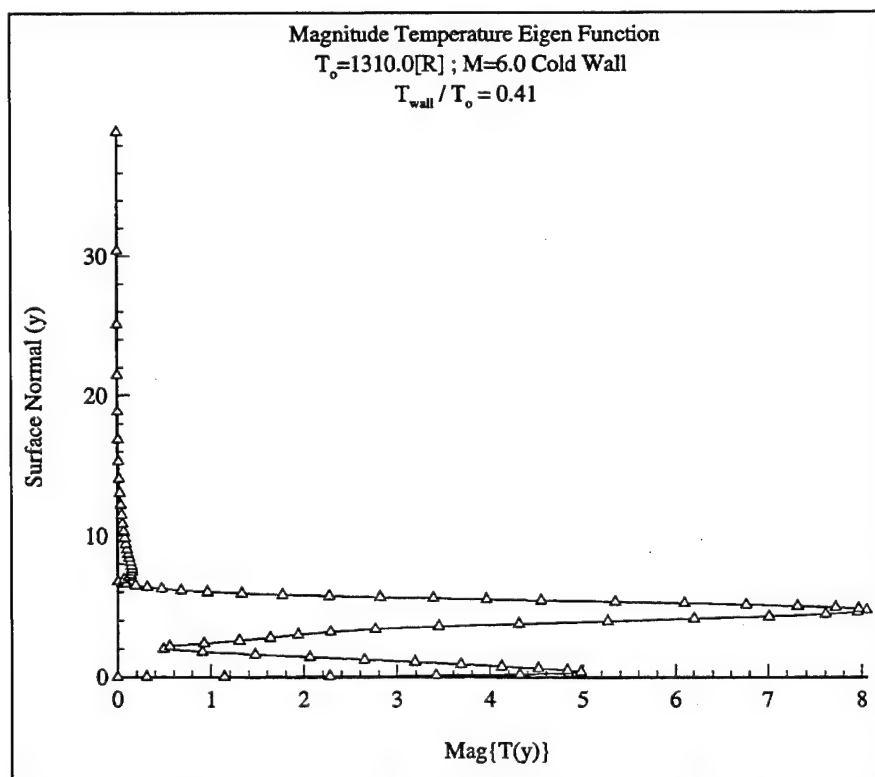


Figure A 14 Temperature eigenfunction,  $M=8.0$ ,  $T_w/T_o=0.41$



**Figure A 15 Temperature eigenfunction,  $M=6.0, T_w/T_o=0.63$**



**Figure A 16 Temperature eigenfunction  $M=6.0, T_w/T_o=0.41$**

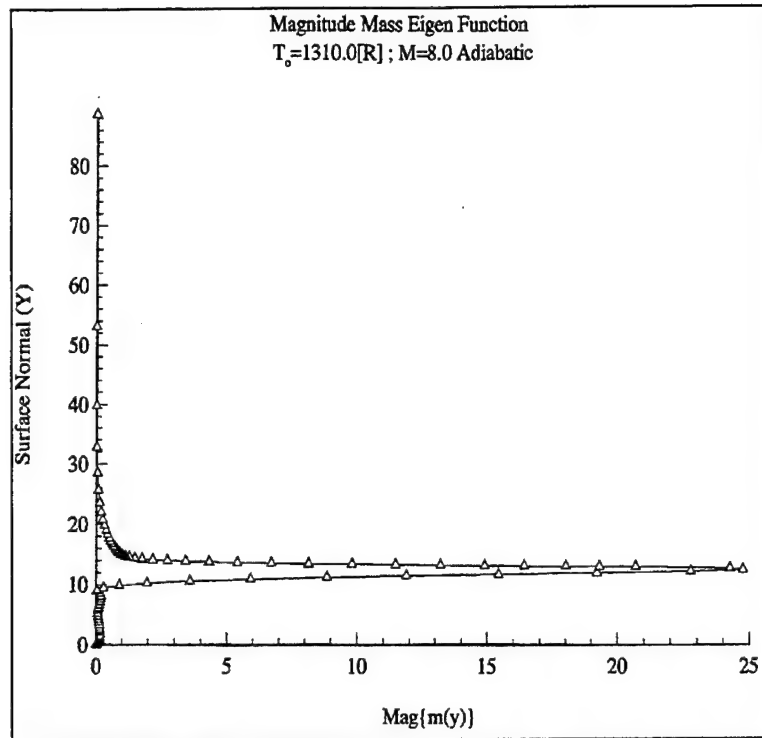


Figure A 17. Mass eigenfunction,  $M=8.0$ , Adiabatic

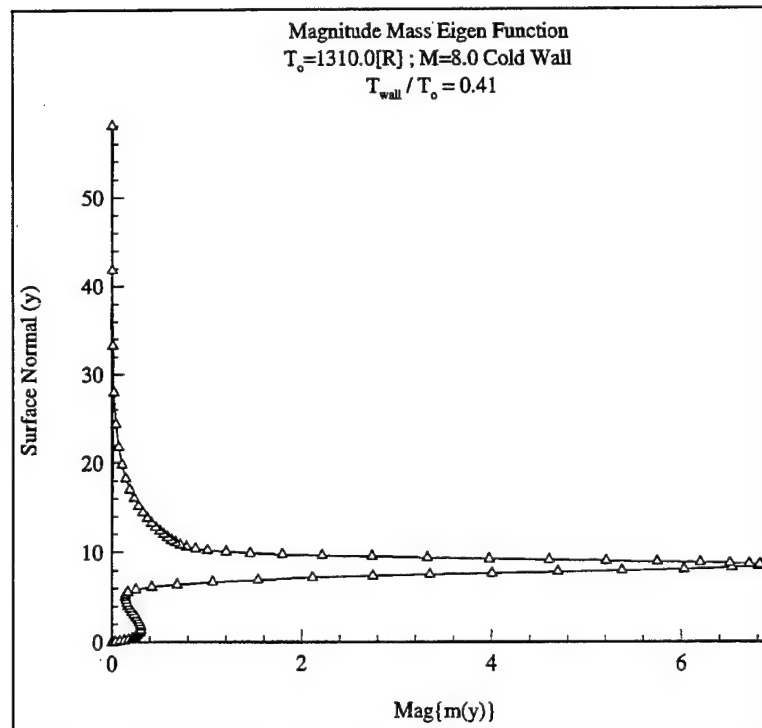
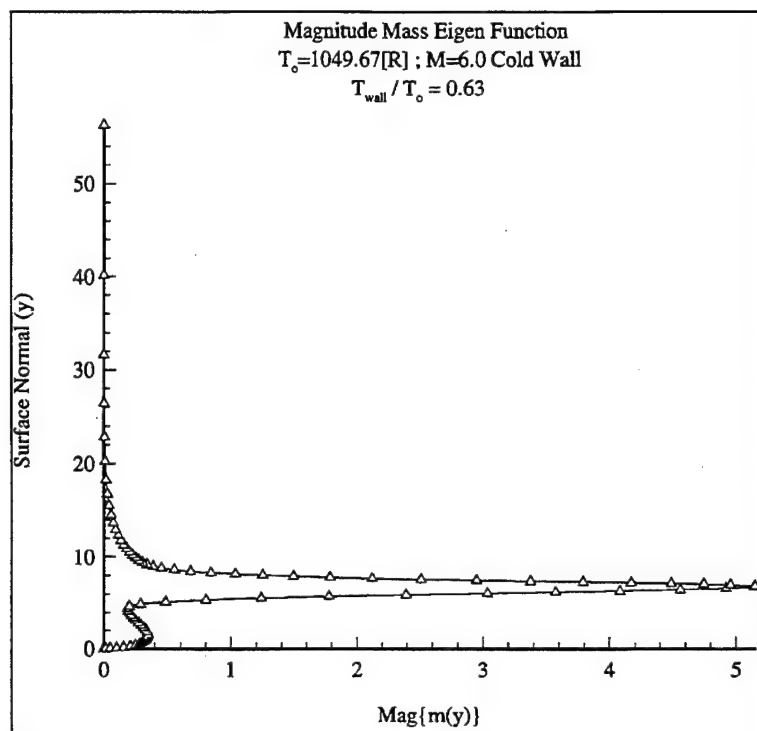
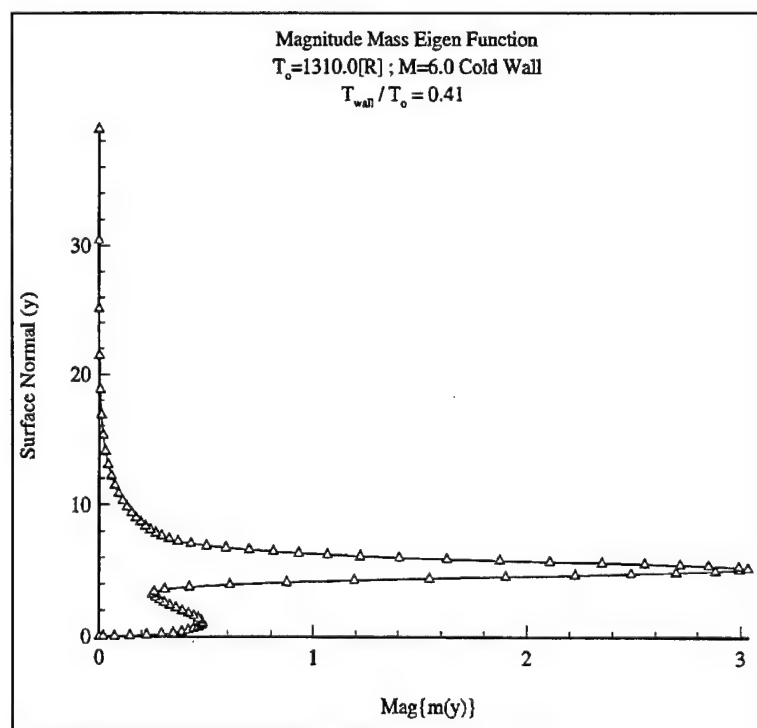


Figure A 18 Mass eigenfunction,  $M=8.0$ ,  $T_w/T_o=0.41$



**Figure A 19 Mass eigenfunction,  $M=6.0$ ,  $T_w/T_o=0.63$**



**Figure A 20 Mass eigenfunction,  $M=6.0$ ,  $T_w/T_o=0.41$**

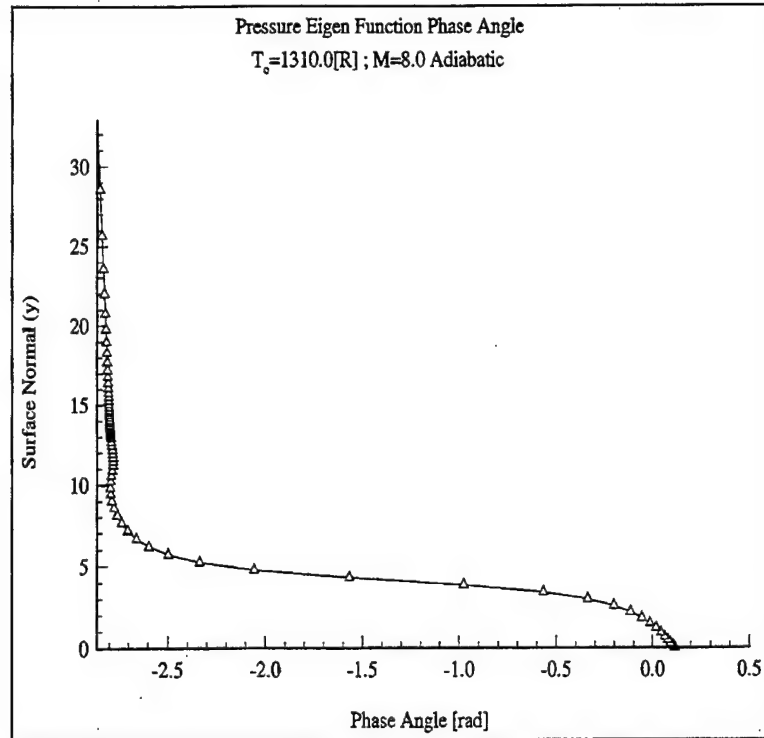


Figure A 21 Pressure function phase angle,  $M=8.0$ , Adiabatic

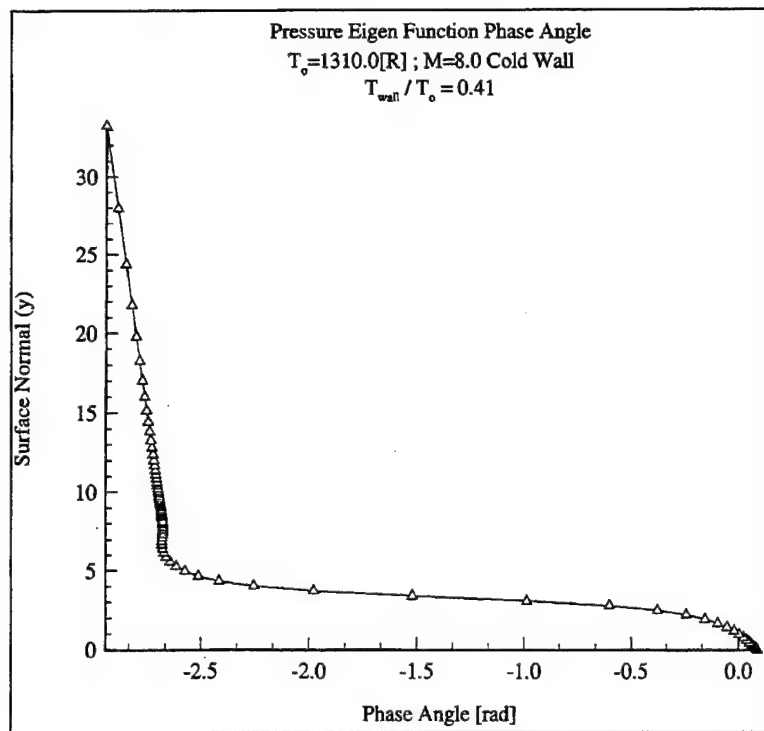
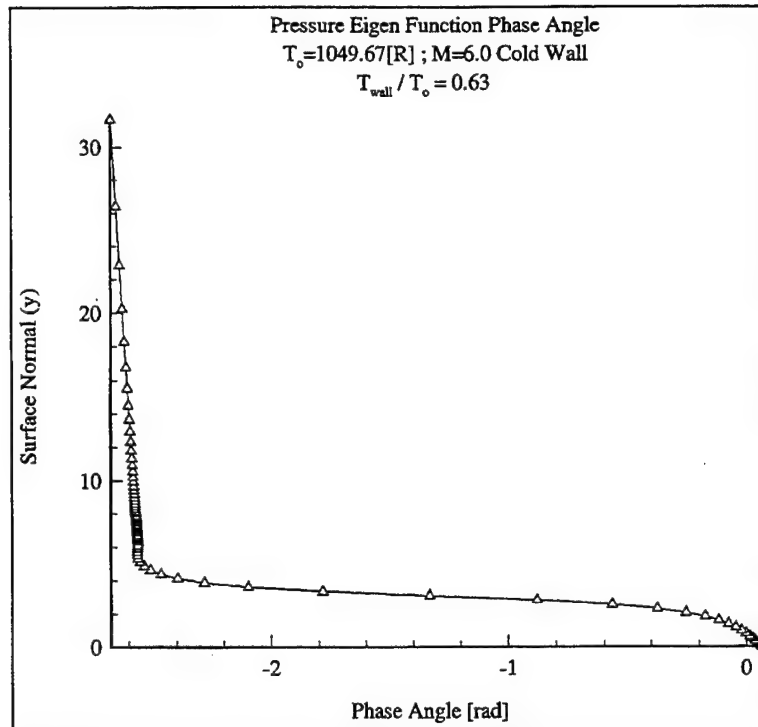
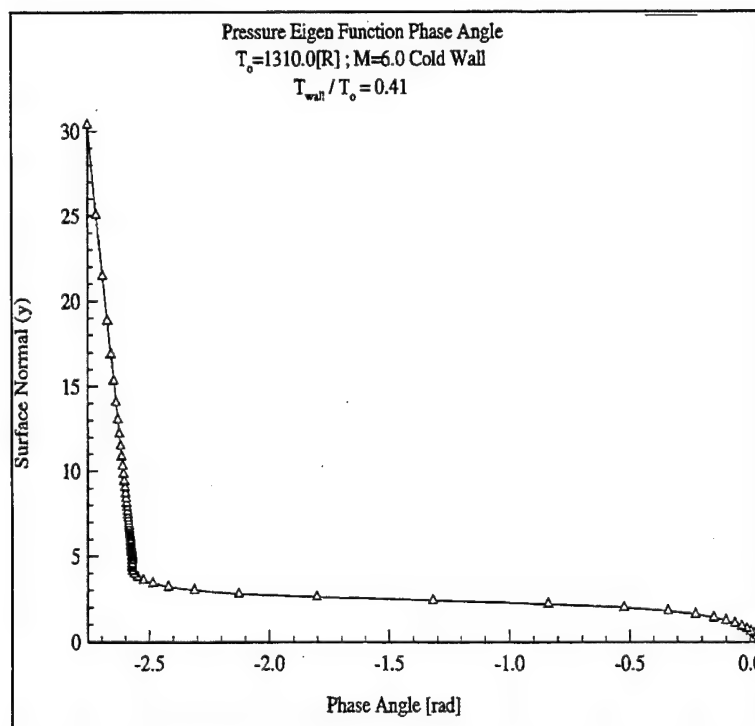


Figure A 22 Pressure function phase angle,  $M=8.0$ ,  $T_w/T_o=0.41$



**Figure A 23 Pressure function phase angle,  $M=6.0$ ,  $T_w/T_o=0.63$**



**Figure A 24 Pressure function phase angle,  $M=6.0$ ,  $T_w/T_o=0.41$**



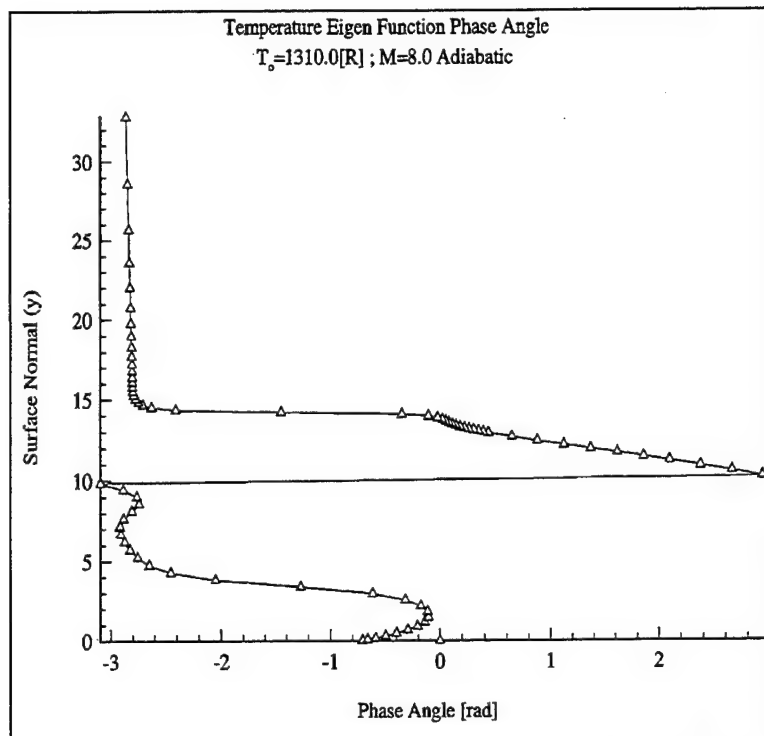


**Figure A 25 Temperature function phase angle,  $M = 8.0$ , Adiabatic**

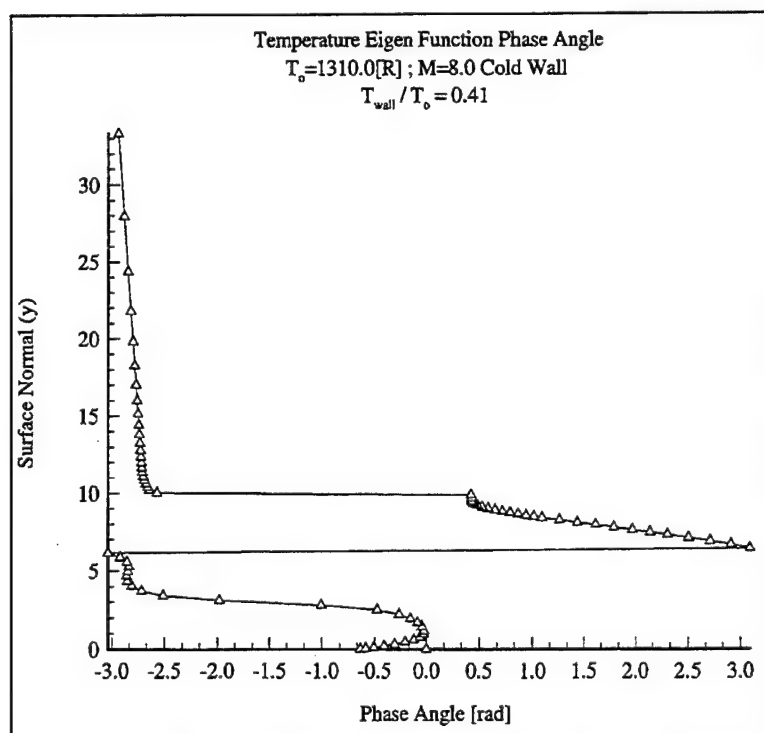


**Figure A 26 Temperature function phase angle,  $M = 8.0$ ,  $T_w/T_o = 0.41$**

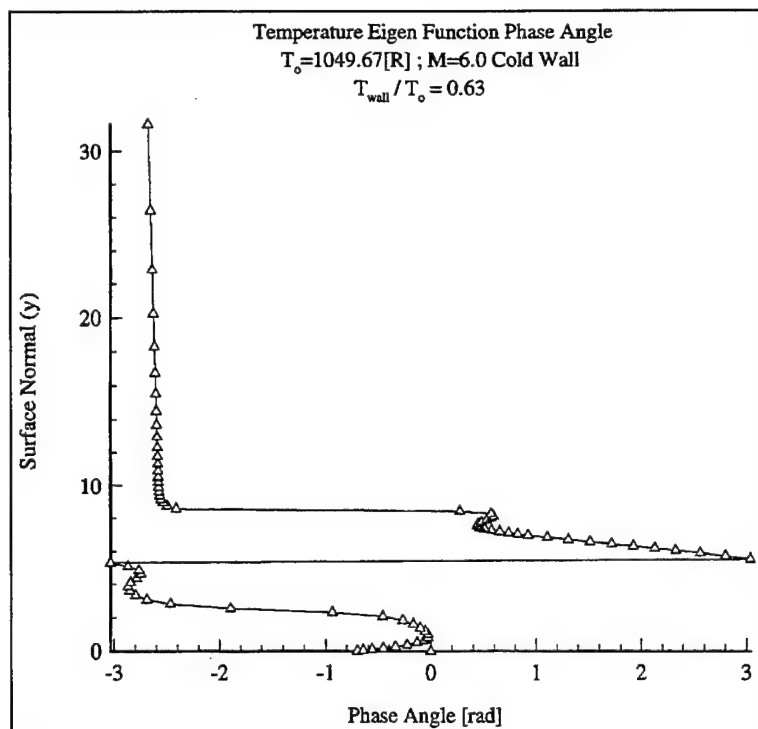


Figure A 27 Temperature function phase angle,  $M = 6.0$ ,  $T_w/T_o = 0.63$

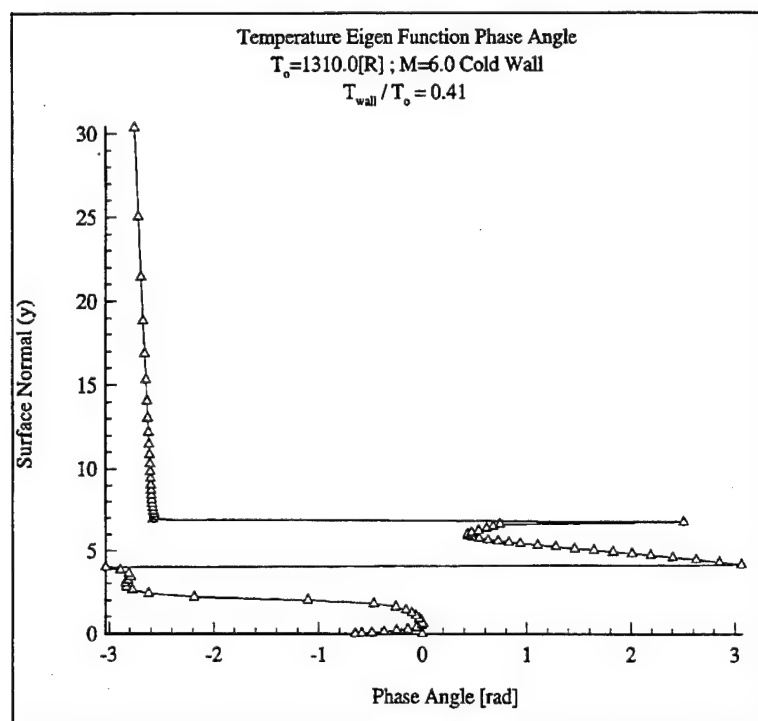


Figure A 28 Temperature function phase angle,  $M = 6.0$ ,  $T_w/T_o = 0.41$

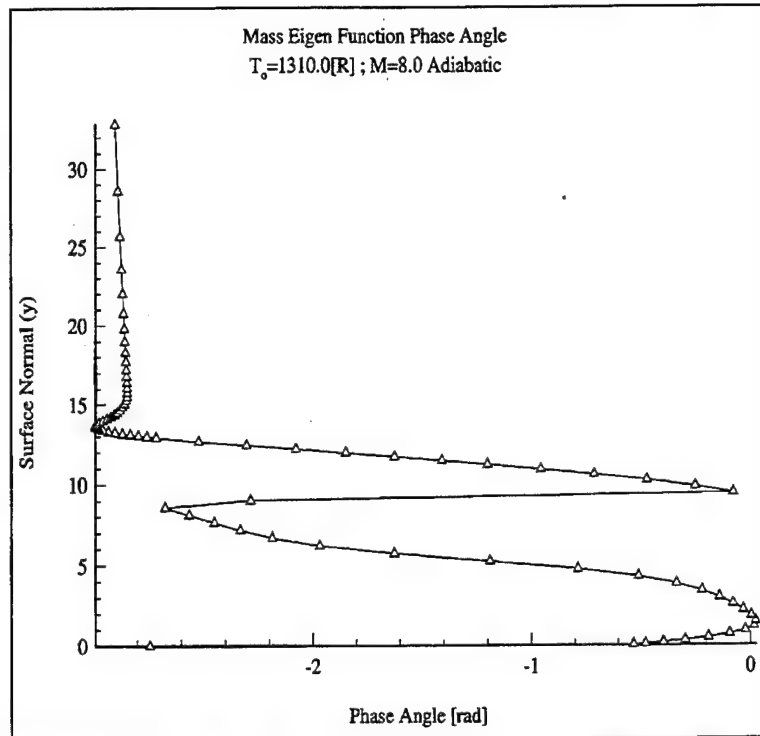


Figure A 29 Mass function phase angle,  $M=8.0$ , Adiabatic

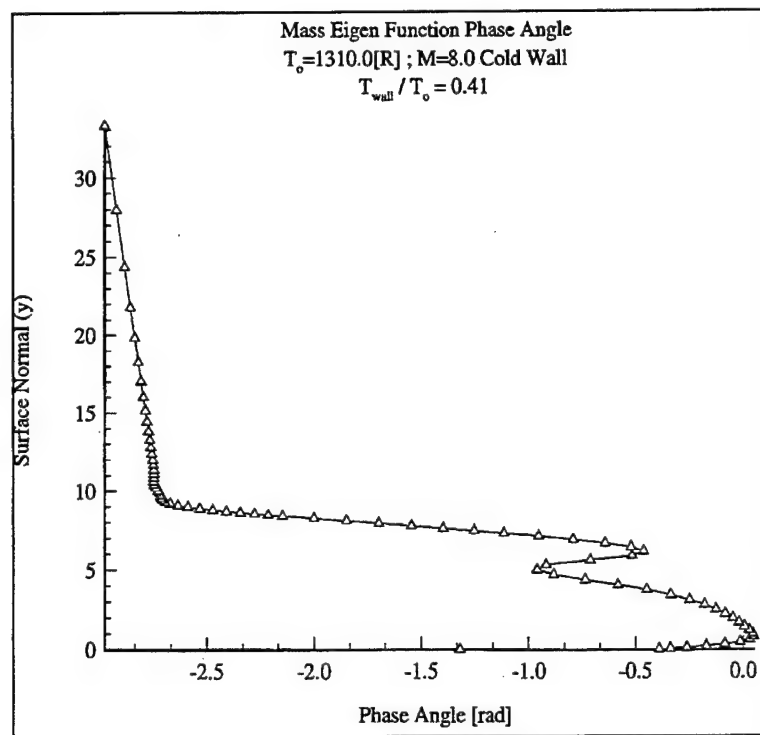


Figure A 30 Mass function phase angle,  $M=8.0$ ,  $T_w/T_o = 0.41$

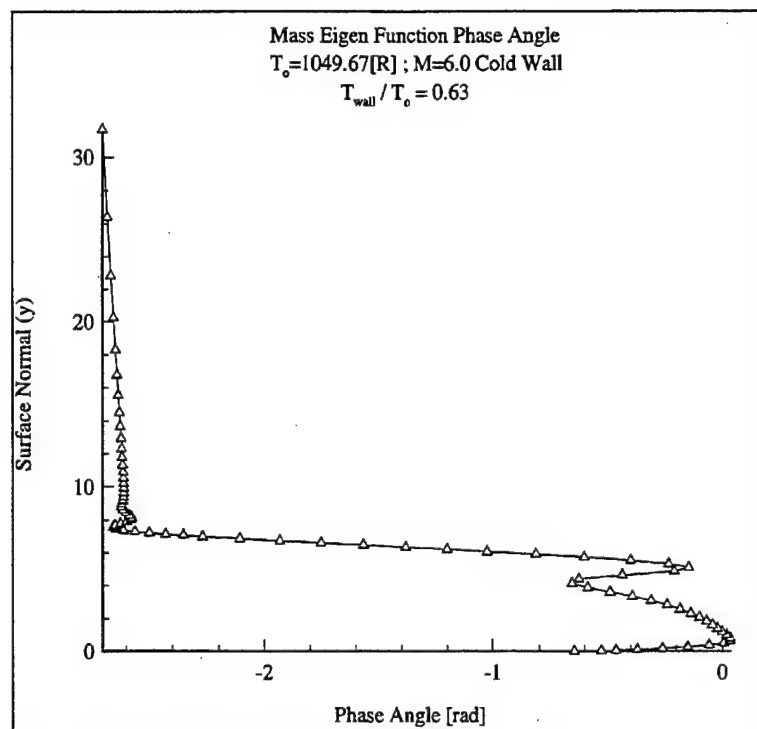


Figure A 31 Mass function phase angle,  $M=6.0$ ,  $T_w/T_o = 0.63$

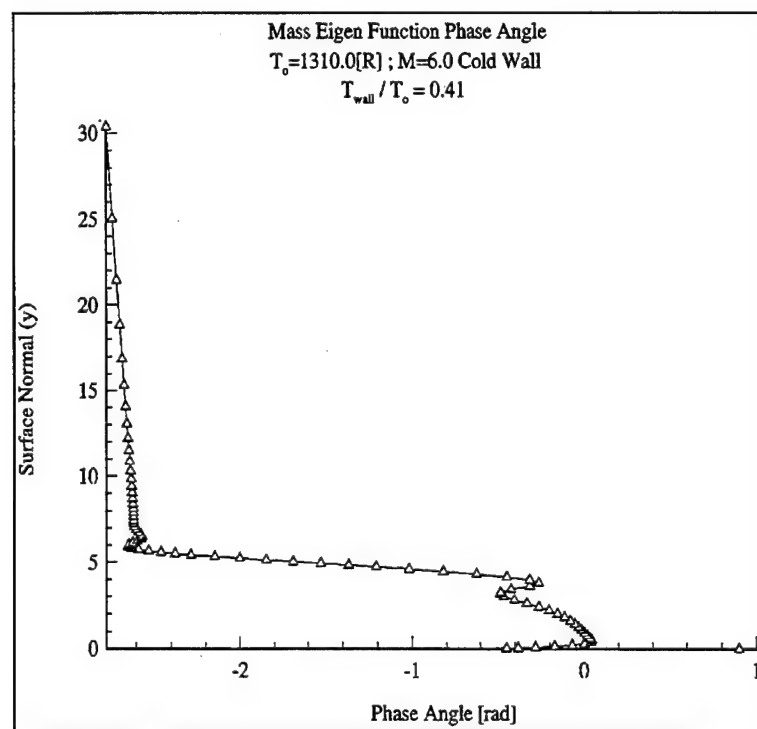


Figure A 32 Mass function phase angle,  $M=6.0$ ,  $T_w/T_o = 0.41$

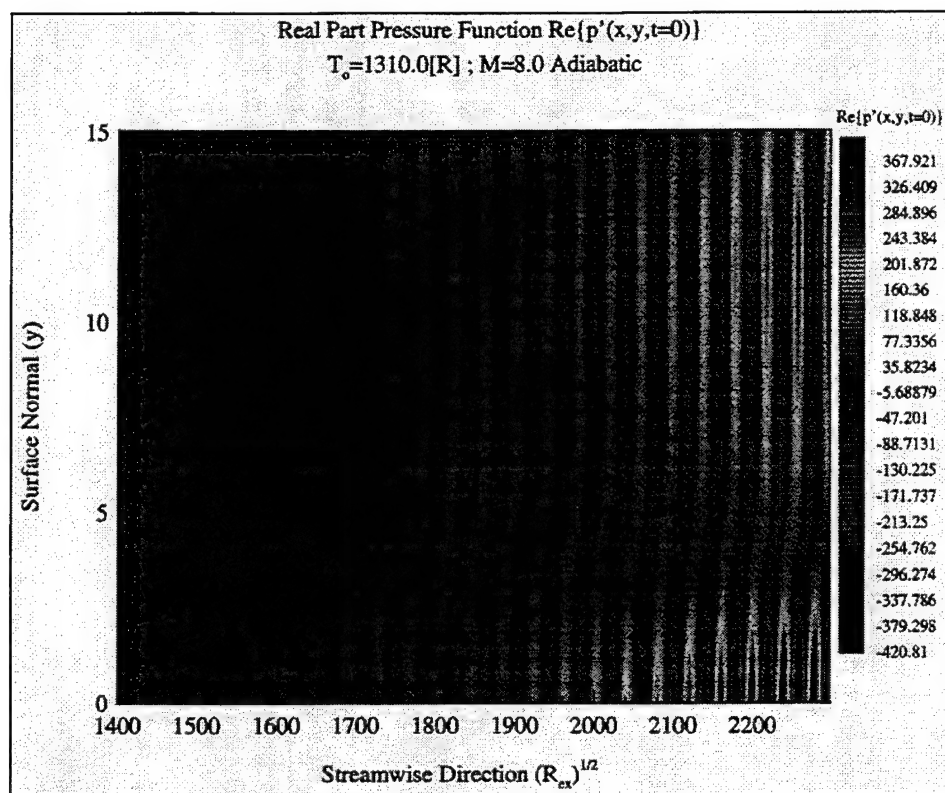


Figure A 33 Real part pressure function,  $M=8.0$ , Adiabatic

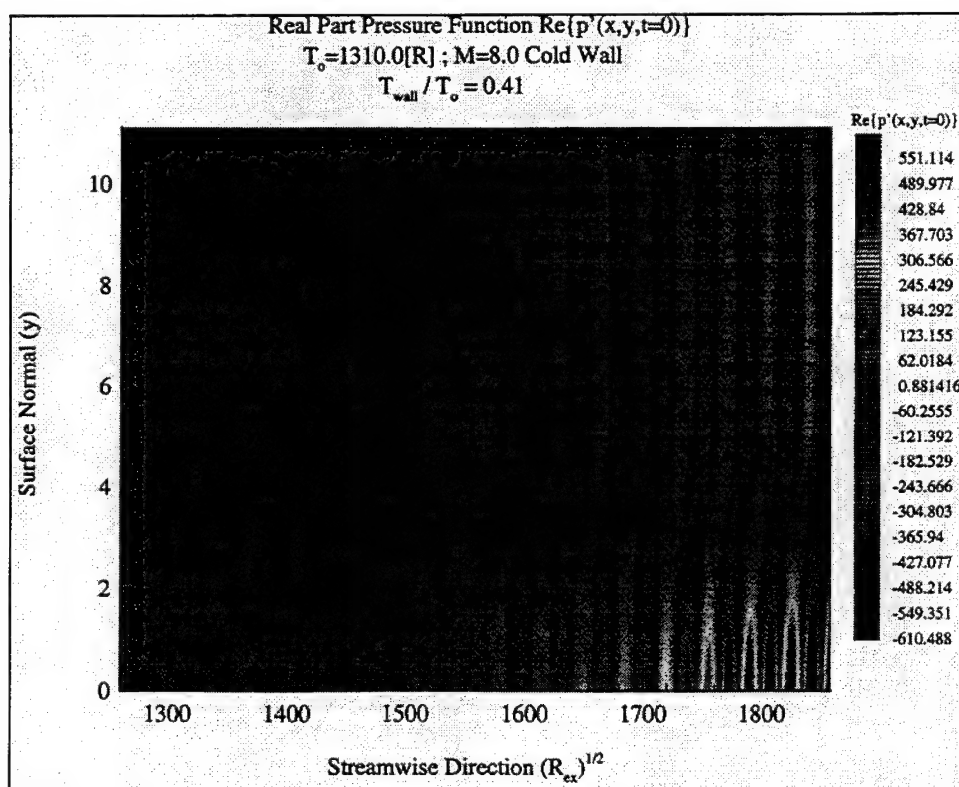


Figure A 34 Real part pressure function,  $M=8.0$ ,  $T_w/T_o = 0.41$

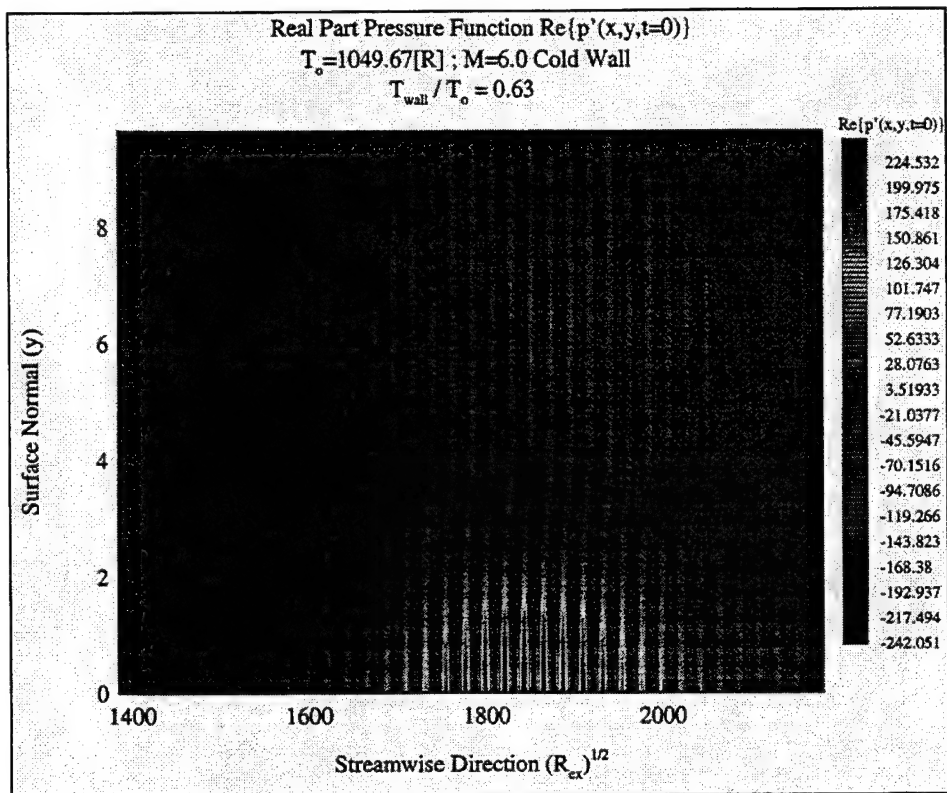


Figure A 35 Real part pressure function,  $M=6.0$ ,  $T_w/T_o = 0.63$

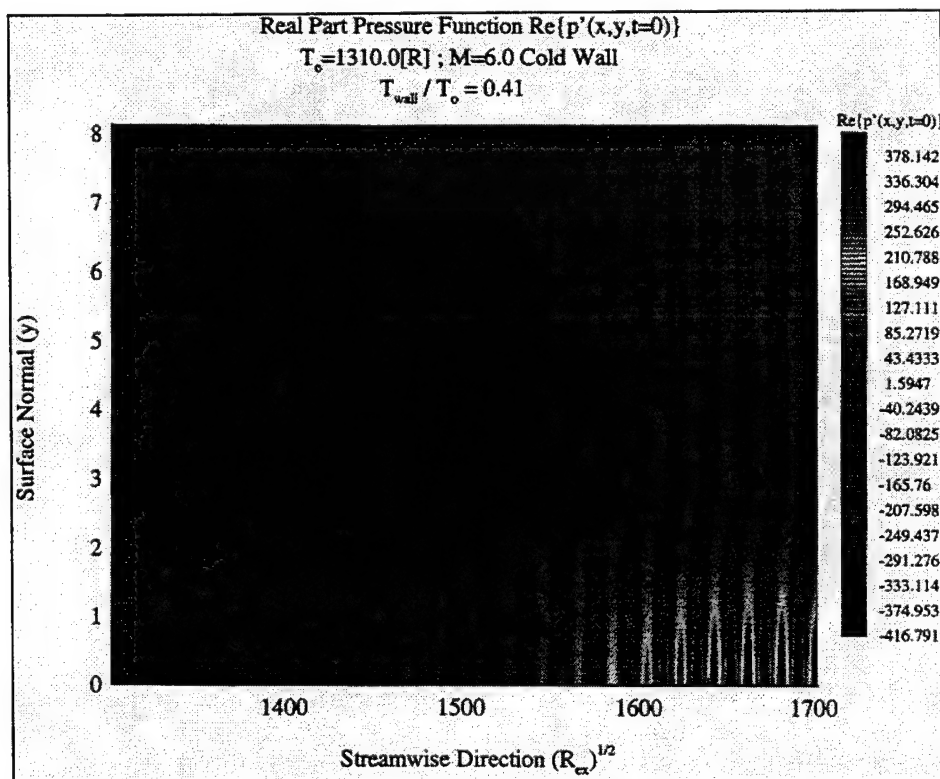


Figure A 36 Real part pressure function,  $M=6.0$ ,  $T_w/T_o=0.41$

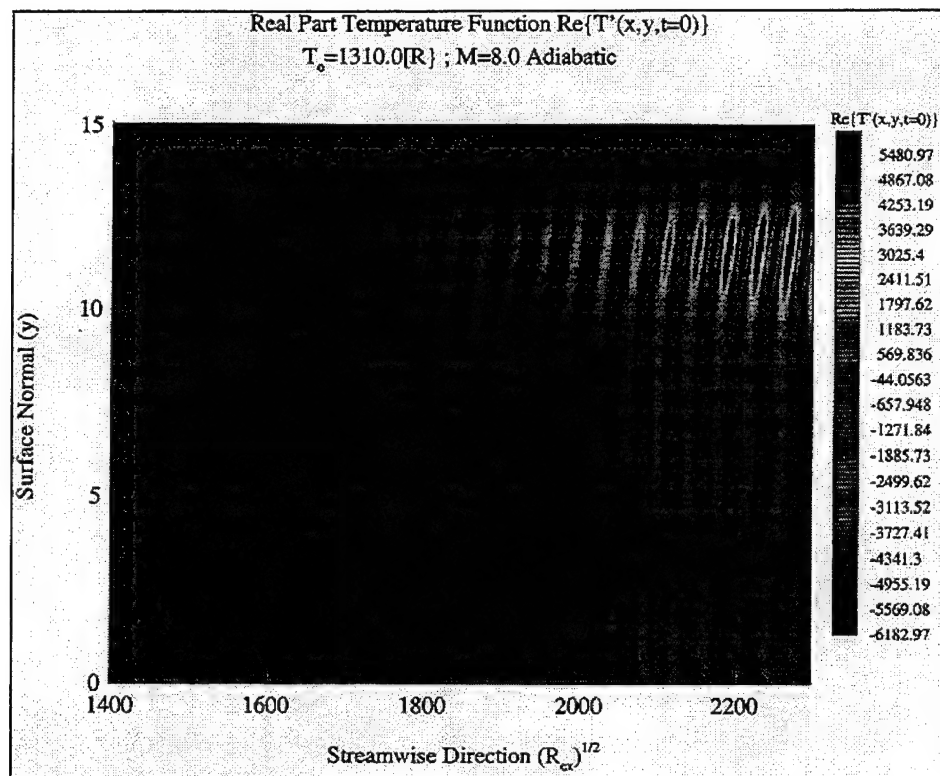


Figure A 37 Real part temperature function,  $M=8.0$ , Adiabatic

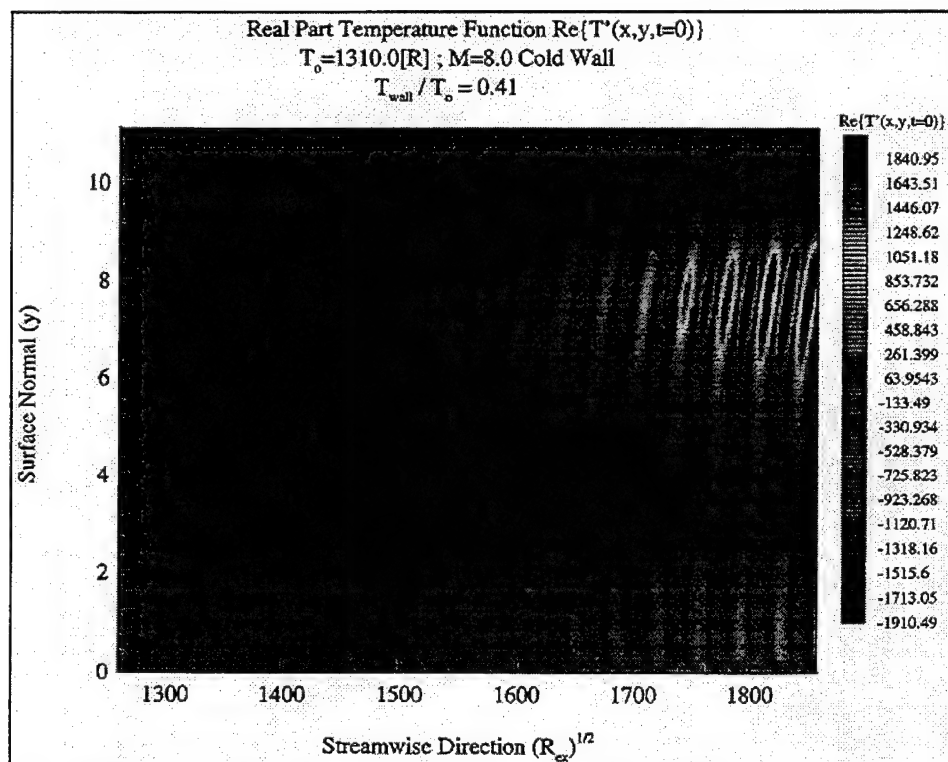


Figure A 38 Real part temperature function,  $M=8.0$ ,  $T_w/T_o = 0.41$

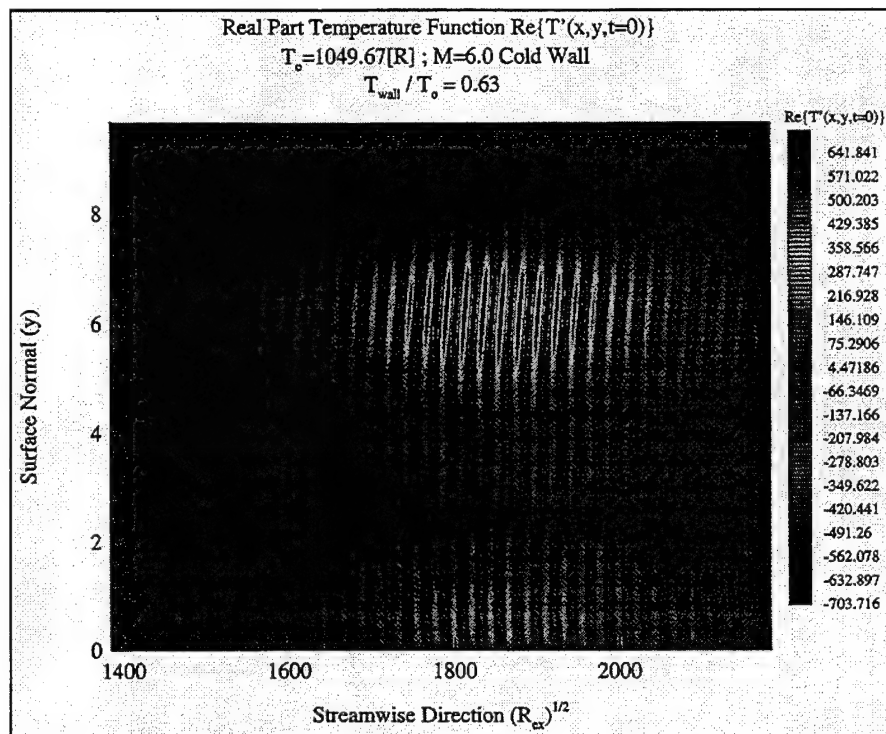


Figure A 39 Real part temperature function,  $M=6.0$ ,  $T_w/T_o = 0.63$

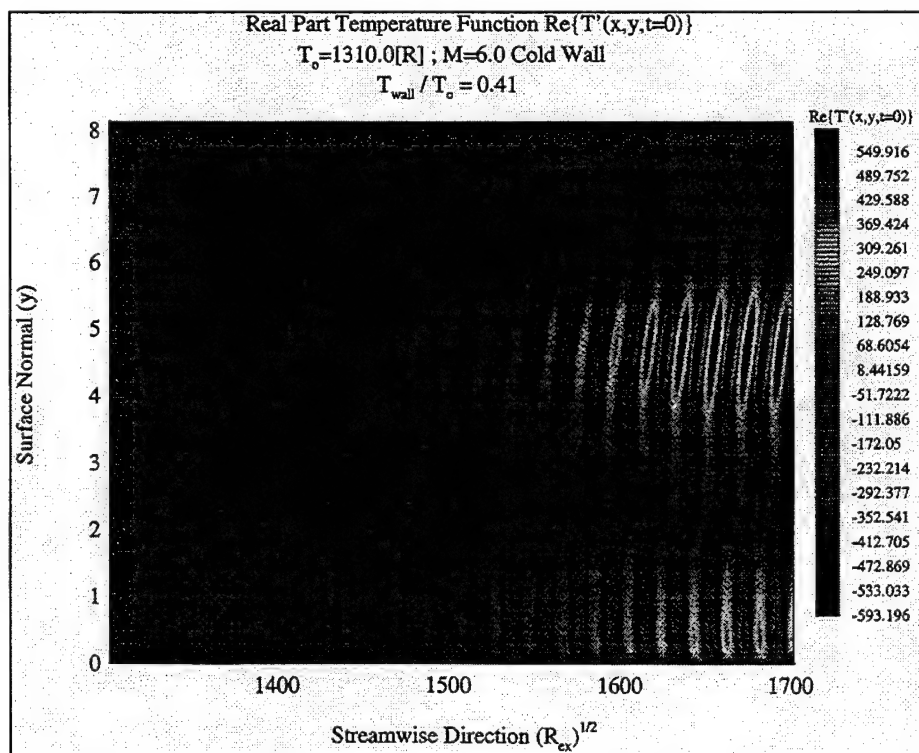


Figure A 40 Real part temperature function,  $M=6.0$ ,  $T_w/T_o = 0.41$



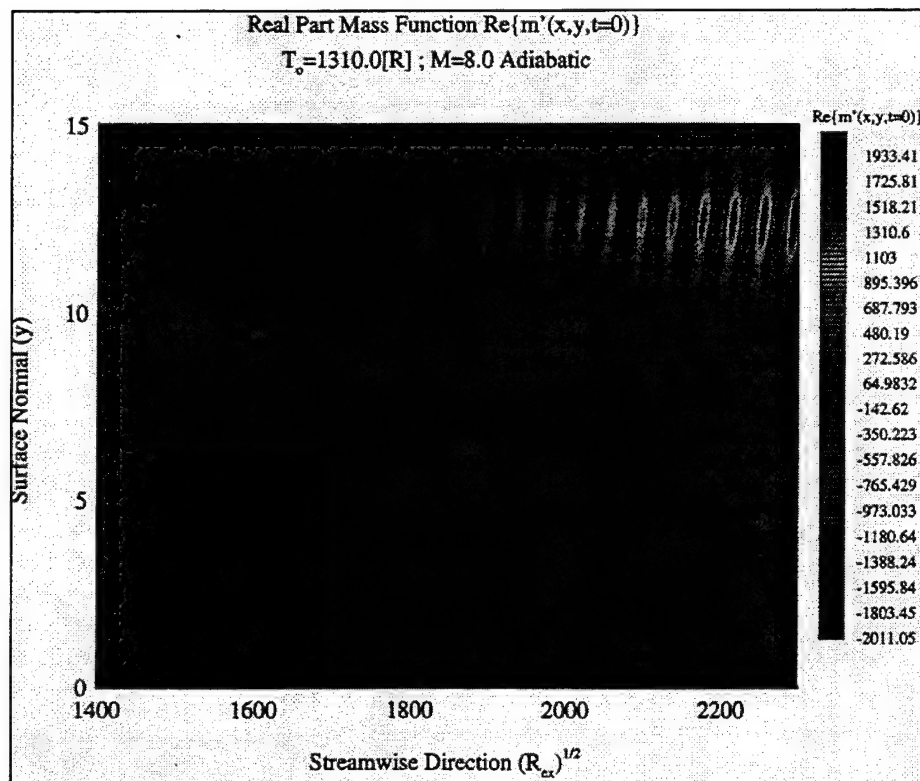


Figure A 41 Real part mass function,  $M=8.0$ , Adiabatic

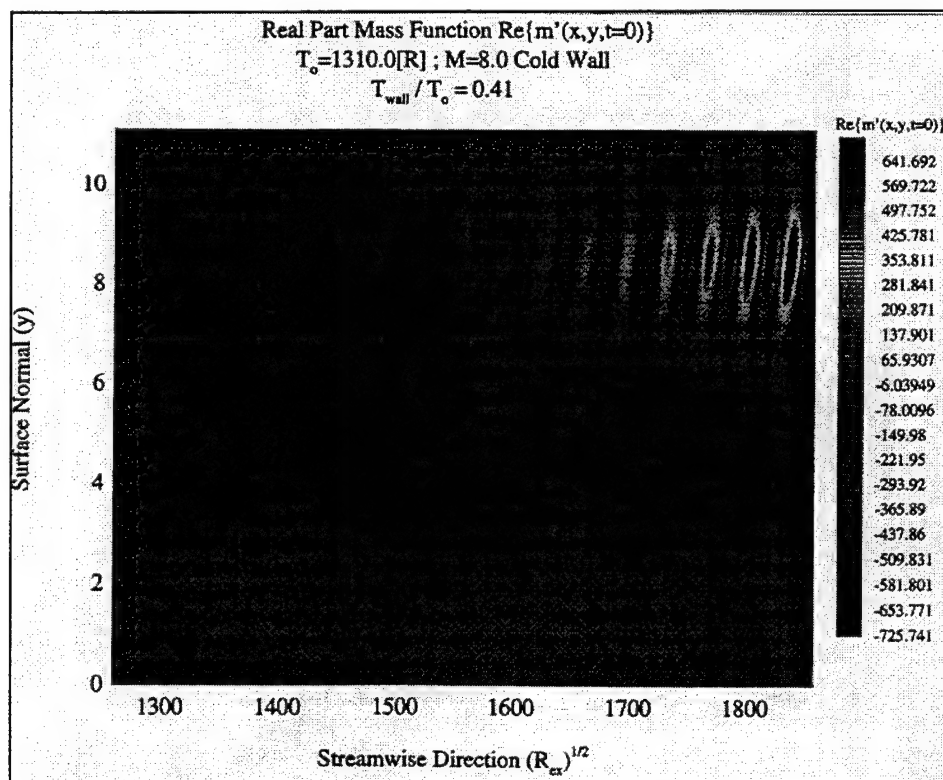


Figure A 42 Real part mass function,  $M=8.0$ ,  $T_w/T_o = 0.41$

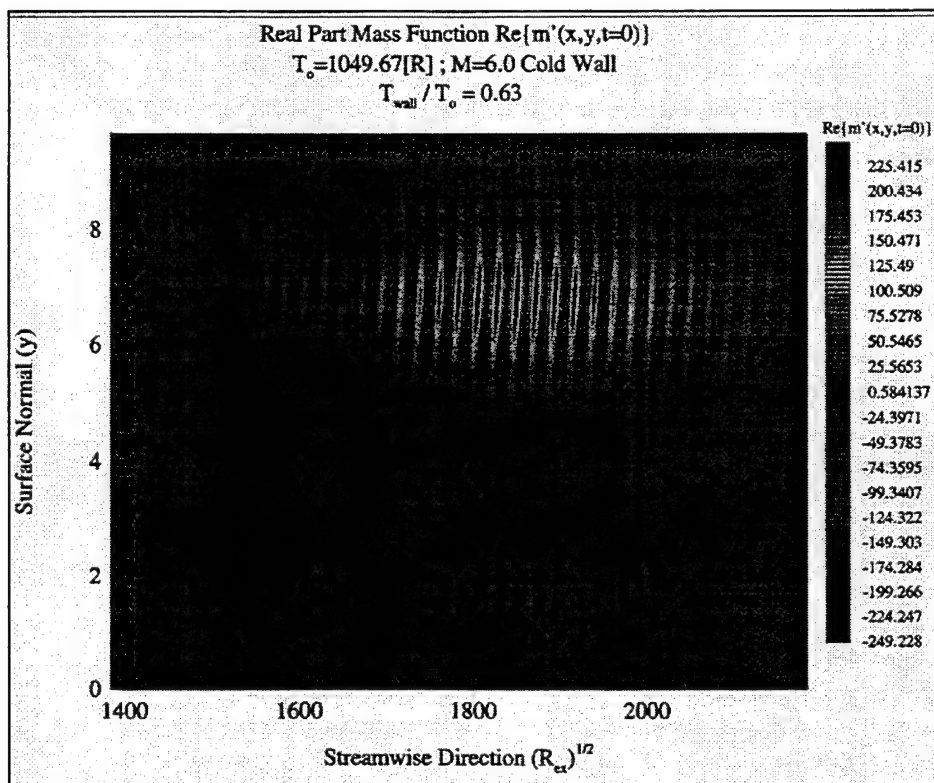


Figure A 43 Real part mass function,  $M=6.0$ ,  $T_w/T_o = 0.63$

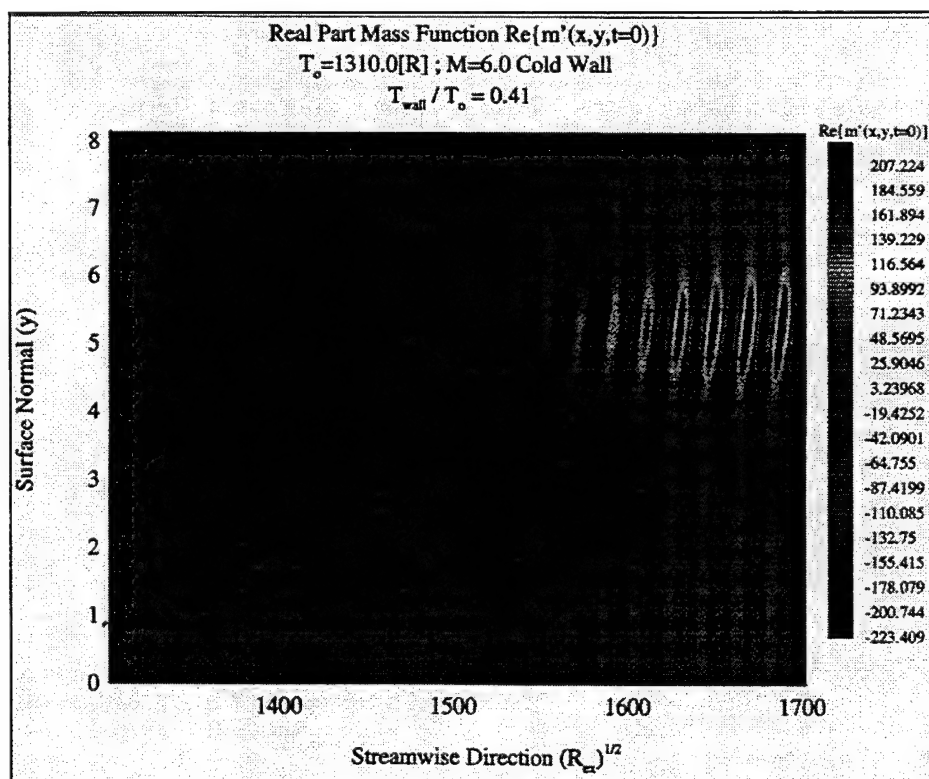


Figure A 44 Real part mass function,  $M=6.0$ ,  $T_w/T_o = 0.41$

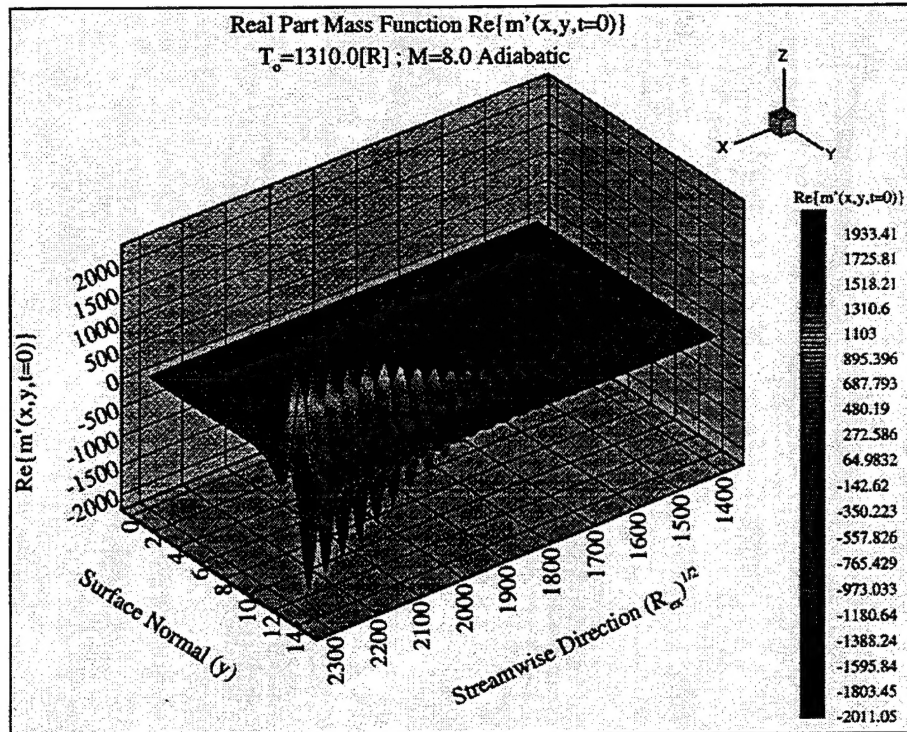


Figure A 45 Real part mass function,  $M=8.0$ , Adiabatic

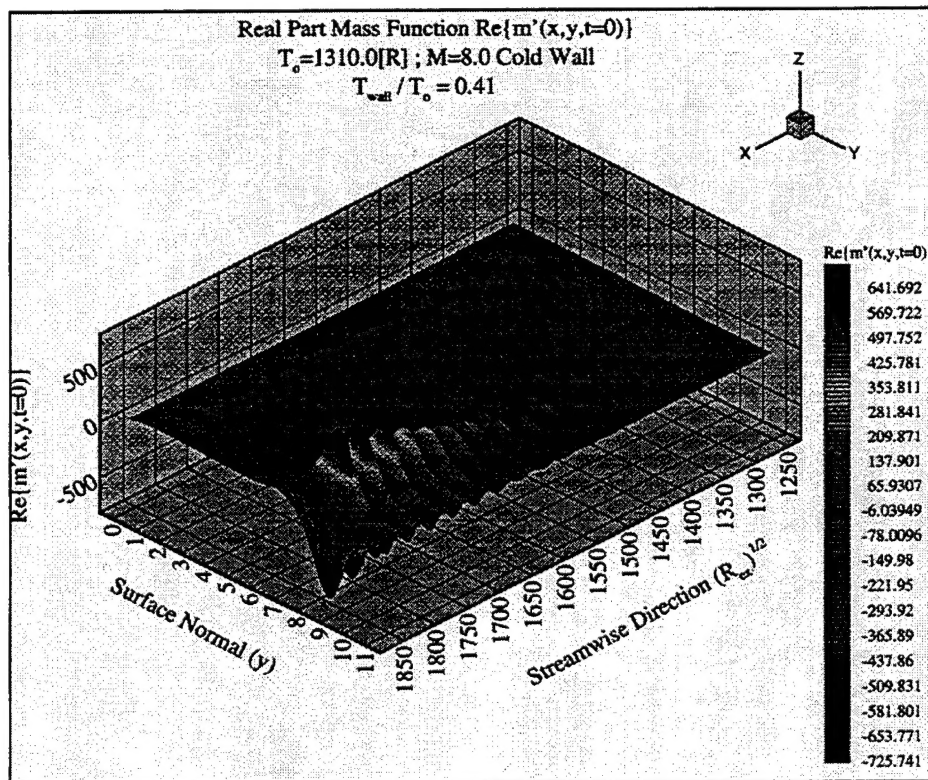


Figure A 46 Real part mass function,  $M=8.0$ ,  $T_w/T_o = 0.41$

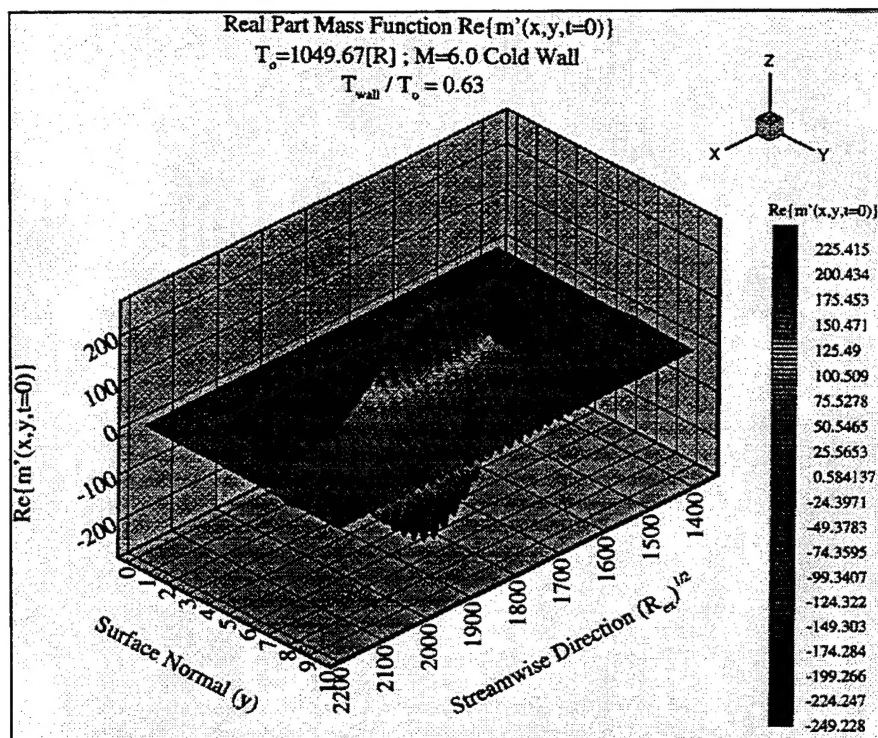


Figure A 47 Real part mass function,  $M=6.0$ ,  $T_w/T_o = 0.63$

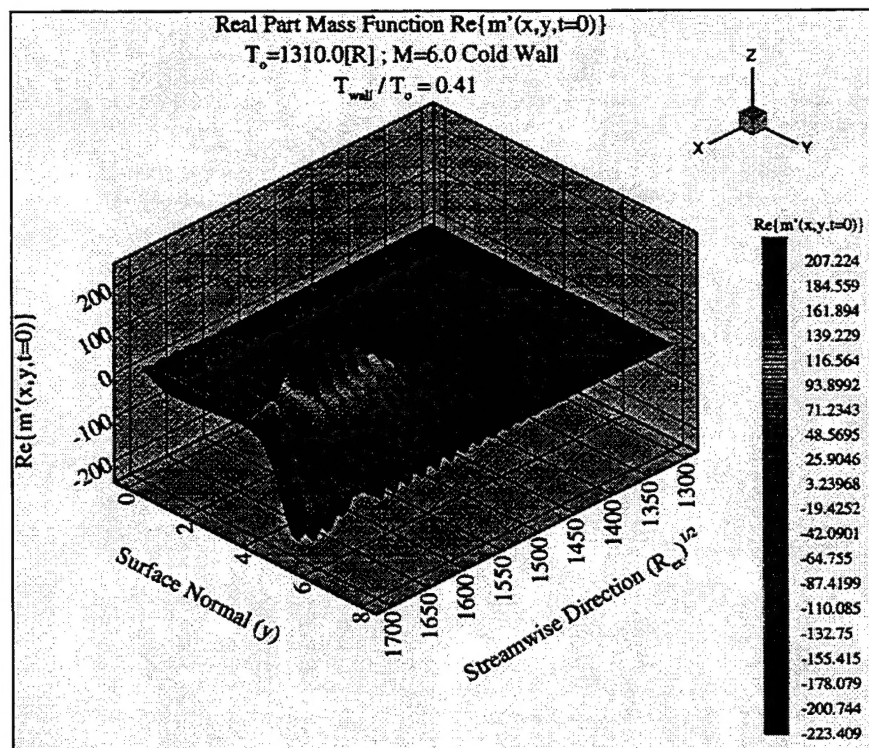


Figure A 48 Real part mass function,  $M=6.0$ ,  $T_w/T_o = 0.41$

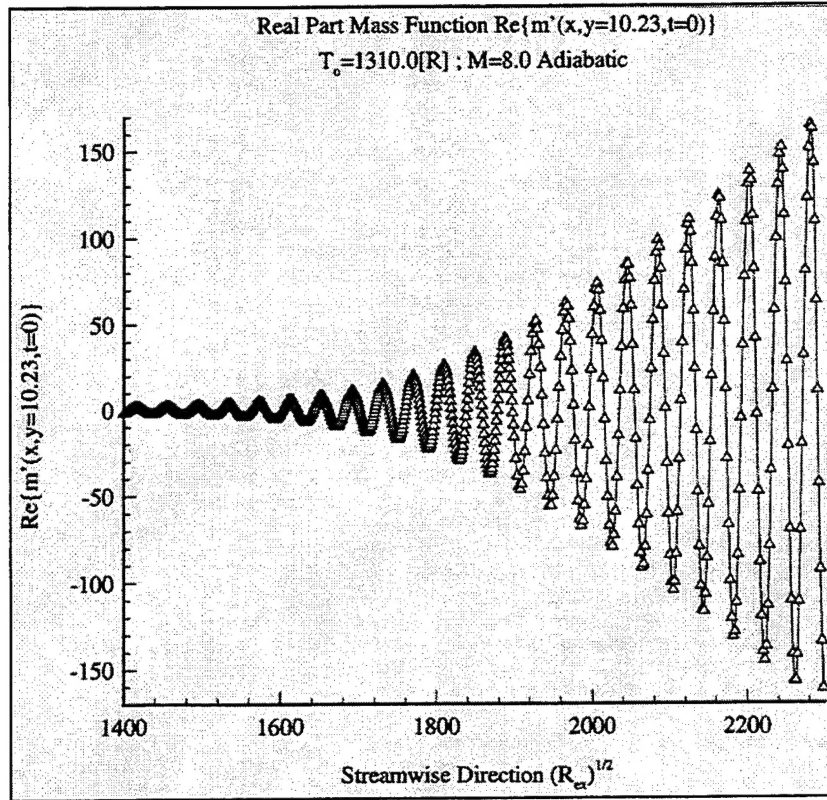


Figure A 49 Real part mass function,  $M=8.0$ , Adiabatic

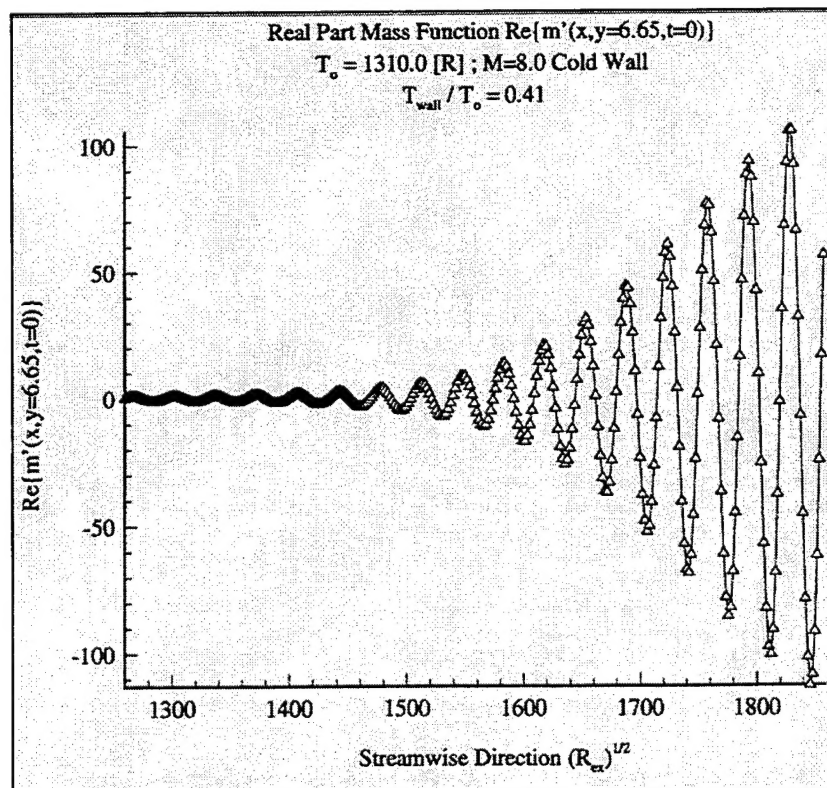


Figure A 50 Real part mass function,  $M=6.0$ ,  $T_w/T_o = 0.41$



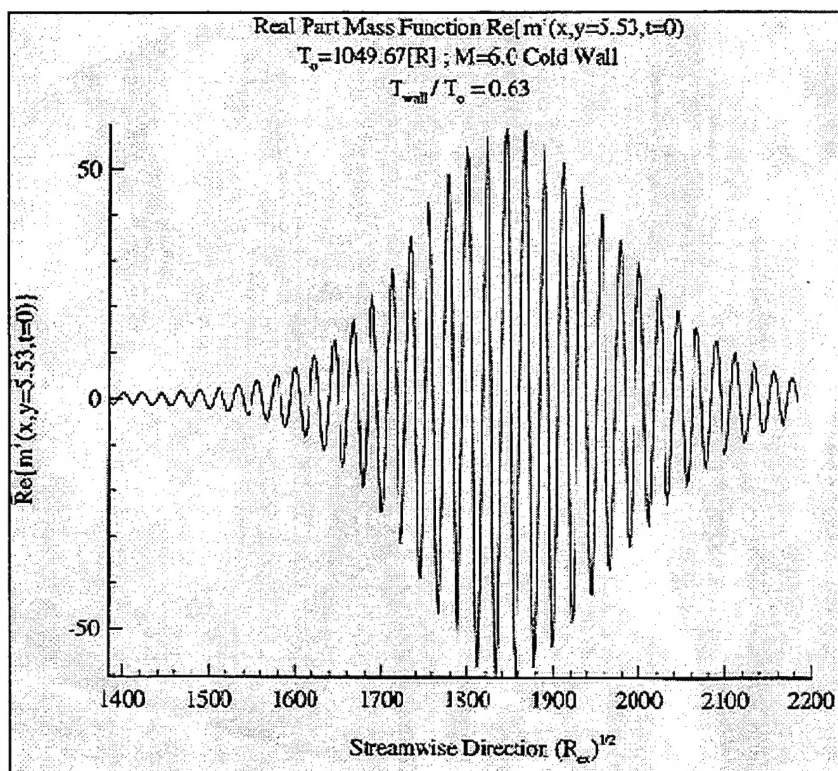


Figure A 51 Real part mass function,  $M=6.0$ ,  $T_w/T_o = 0.63$

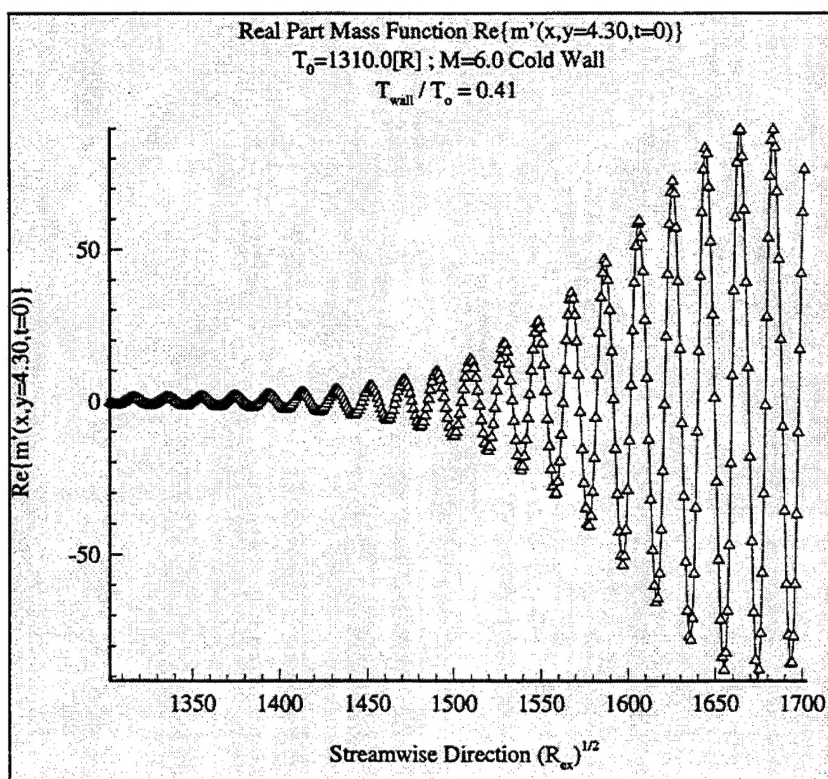


Figure A 52 Real part mass function,  $M=6.0$ ,  $T_w/T_o = 0.41$